Monthly Notices of the ROYAL ASTRONOMICAL SOCIETY

MNRAS **525,** 1061–1076 (2023) https://doi.org/10.1093/mnras/stad2394
Advance Access publication 2023 August 08

SIMBA-C: an updated chemical enrichment model for galactic chemical evolution in the SIMBA simulation

Renier T. Hough [1]★ Douglas Rennehan [2] Chiaki Kobayashi [3] S. Ilani Loubser [1,4] Romeel Davé,[5,6] Arif Babul[7] and Weiguang Cui [4,8,9]

[1]*Centre for Space Research, North-West University, Potchefstroom 2520, South Africa*
[2]*Center for Computational Astrophysics, Flatiron Institute, 162 5th Ave, New York, NY 10010, USA*
[3]*Centre for Astrophysics Research, Department of Physics, Astronomy and Mathematics, University of Hertfordshire, Hatfield AL10 9AB, UK*
[4]*National Institute for Theoretical and Computational Sciences (NITheCS), Potchefstroom 2520, South Africa*
[5]*School of Physics and Astronomy, University of Edinburgh, Edinburgh EH9 3HJ, UK*
[6]*Department of Physics and Astronomy, University of the Western Cape, Bellville 7535, South Africa*
[7]*Department of Physics and Astronomy, University of Victoria, Victoria BC V8P 5C2, Canada*
[8]*Departamento de Física Teórica, M-8, Universidad Autónoma de Madrid, Cantoblanco, E-28049 Madrid, Spain*
[9]*Centro de Investigación Avanzada en Física Fundamental (CIAFF), Universidad Autónoma de Madrid, Cantoblanco, E-28049 Madrid, Spain*

Accepted 2023 August 2. Received 2023 July 26; in original form 2023 April 28

ABSTRACT

We introduce a new chemical enrichment and stellar feedback model into GIZMO , using the SIMBA sub-grid models as a base. Based on the state-of-the-art chemical evolution model of Kobayashi et al., SIMBA-C tracks 34 elements from H→Ge and removes SIMBA's instantaneous recycling approximation. Furthermore, we make some minor improvements to SIMBA's base feedback models. SIMBA-C provides significant improvements on key diagnostics such as the knee of the $z = 0$ galaxy stellar mass function, the faint end of the main sequence, and the ability to track black holes in dwarf galaxies. SIMBA-C also matches better with recent observations of the mass–metallicity relation at $z = 0, 2$. By not assuming instantaneous recycling, SIMBA-C provides a much better match to galactic abundance ratio measures such as [O/Fe] and [N/O]. SIMBA-C thus opens up new avenues to constrain feedback models using detailed chemical abundance measures across cosmic time.

Key words: software: simulations – supernovae: general – ISM: abundances – galaxies: abundances – galaxies: evolution – galaxies: formation.

1 INTRODUCTION

Studying the large-scale structure of the Universe, specifically the formation of galaxies, groups of galaxies, and clusters of galaxies and how they evolve over time, can give us insight into the inner workings of how the Universe formed and evolved (Dolag et al. 2008). Numerical simulations can help us to visualize and understand the key physical processes involved in galaxy and other large-scale structure evolution.[1] One such process is the rate at which stars form.

It is well documented that free-falling cool gas leads to the formation of stars (Kennicutt Robert C. et al. 2007; Leroy et al. 2008). However, this alone cannot account for the observed rate at which stars are formed (Rasia et al. 2015). We know that cold metal-free gas ($T < 10^4$ K) cooling solely through rotational-vibrational lines of H_2 has a minimum achievable temperature of ~ 200 K (Smith et al. 2009). The energy levels of H_2 become thermalized at low densities ($n \sim 10^3 - 10^4\,\mathrm{cm}^{-3}$), above which the cooling rate is $\propto n$ (Bromm, Coppi & Larson 2002; Smith et al. 2009). This leads to a stalling point in the star formation process as the gas cooling time increases above the dynamical time (Abel, Bryan & Norman 2002; Stinson et al. 2013).

Other processes must therefore be involved. The first process is metal-cooling, where metals are created in stars through the nucleosynthesis processes, due to the early star formation from metal-free cold gas. These metals then provide more available atomic and molecular transitions, allowing the gas to lose its internal energy faster than in the metal-free case (Smith, Sigurdsson & Abel 2008). This reduces the gas cooling time to be shorter than the dynamical time and star formation can proceed again. Therefore, metals within cold collapsing gas clouds increase the efficiency of star formation (Kobayashi, Springel & White 2007; Smith et al. 2009). However, this will result in a star formation rate (SFR) that can be higher than observed (Stinson et al. 2013; Rasia et al. 2015), in turn leading to too many old spheroidal galaxies at $z = 0$ (White & Frenk 1991; Piontek & Steinmetz 2011).

Therefore processes, called feedback, e.g. supernovae (SNe) and active galactic nuclei (AGNs), are needed to re-heat the gas (Piontek & Steinmetz 2011; Stinson et al. 2013). These processes inject massive amounts of energy into the cold collapsing gas clouds, which

★ E-mail: renierht@gmail.com

[1]For more insight into these simulations, we refer the reader to (Bertschinger 1998; Springel, Frenk & White 2006; Dolag et al. 2008; Davé, Oppenheimer & Finlator 2011; Hahn & Abel 2011; Somerville & Davé 2015; Naab & Ostriker 2017; Vogelsberger et al. 2020; Hough et al. 2021; Oppenheimer et al. 2021; Jung et al. 2022; Kobayashi & Taylor 2023).

increases the temperature and stalls star formation. This quenching of star formation can be seen in the famous SFR versus cosmic time result from Madau & Dickinson (2014) after the SFR reached a peak at $z \sim 2$, called Cosmic High Noon (Mehta et al. 2017). However, events such as stellar winds and SNe inject new types of metals, leading to a self-regulating cycle between star formation and feedback.[2]

Studying the chemical composition of these newly created and injected metals within galaxies can provide us with powerful insights into all of the factors discussed above, i.e. star formation efficiency, gas inflow rate, and metal-rich gas outflow rate (Maiolino & Mannucci 2019; Beverage et al. 2023). Furthermore, the composition of the stellar content of galaxies contains the integrated enrichment of the gas over its entire star formation history (Cameron & Truran 1971). This is particularly true for stellar abundances in quiescent galaxies, which have prominent absorption features.

Two of the well-known properties of massive quiescent galaxy properties are: (i) The most massive local quiescent galaxies contain the most metals (Kobayashi & Arimoto 1999; Gallazzi et al. 2005; Thomas et al. 2005; Beverage et al. 2023). This is thought to be a reflection of the strength of the gravitational potential of the host galaxy–SNe and stellar winds are less effective at removing metals from the gas in deep potential wells (Larson 1974; Tremonti et al. 2004; Liang et al. 2016; Beverage et al. 2023); (ii) Massive quiescent galaxies are the oldest and most enriched in α-elements, log ([α/Fe]) (Thomas et al. 2005; Spolaor et al. 2010; Conroy, Graves & van Dokkum 2014; McDermid et al. 2015; Beverage et al. 2023). This is an indication of the relative enrichment due to core-collapse or delayed Type 1a SNe, directly probing the SFR time-scales within the galaxy (Matteucci 1994; Rennehan et al. 2020).

Even from these two examples one can understand why the study of galactic chemical enrichment is a powerful probe that one can use in our numerical simulations to give us insight into the evolution of galaxies. Therefore, tracking the chemical enrichment and its stellar feedback counterpart as accurately as possible is a necessity.

In this paper, we incorporate a new stellar feedback and chemical enrichment model into the SIMBA cosmological simulation (Davé et al. 2019), which is named SIMBA-C. This is done to improve the simplified nature of the existing enrichment model, namely the instantaneous recycling of the metals model approximation. The instantaneous recycling model uses the assumption that all stars more massive than $1 M_\odot$ die instantaneously, while all stars less massive live forever to be able to define the yield per stellar generation y_i and the returned fraction R of the mass ejected into the interstellar medium (ISM) (Matteucci 2016). We provide a more realistic cosmic chemical enrichment model in the simulation that improves the number of elements that can be formed and track these elements more accurately in the simulation. The simplified models tend to track only eleven elements (H, He, C, N, O, Ne, Mg, Si, S, Ca, and Fe), and neglect all other elements (Davé, Thompson & Hopkins 2016; Davé et al. 2019). Our new model also includes more types of stellar feedback events in addition to the event types already included. Finally, we also improve on the instantaneous recycling approximation that is common practice in simplified enrichment models, to be more self-consistent and to take into account the current state of the star particle within the simulation in its evolution. Using the method in Kobayashi (2004), we, therefore, treat the star particles within the simulation as evolving star particles rather than just allowing them to randomly experience stellar feedback processes to create the right amount of metals.

In this paper, Section 2 discusses the input physics of the SIMBA-C model, which is highly dependent on SIMBA, with significant modification in the chemical enrichment and feedback modules. In Section 3, we study the global galaxy properties, including stellar, star formation, and enrichment properties, particularly abundance ratios, which are substantially improved in SIMBA-C relative to SIMBA. Lastly, we describe our conclusions in Section 4.

2 SIMULATION METHODOLOGY

2.1 SIMBA

Our new SIMBA-C simulations are based on the SIMBA simulation (Davé et al. 2019). The SIMBA simulation is a large-volume cosmological simulation that uses the hydrodynamics + gravity solver GIZMO (Springel 2005; Hopkins 2015, 2017). While we summarize the SIMBA model in this section, we point the interested reader to Davé et al. (2019) for further details, while highlighting the changes made in SIMBA-C. GIZMO evolves the hydrodynamic equations using the mesh-free finite mass method and handles shocks using a Riemann solver without artificial viscosity. It also preserves the mass within each fluid element at simulation time, thereby enabling simple tracking of gas flows. Therefore, it marries the advantages of a particle-based code, such as adaptivity in space and time, with the precision of a Riemann solved-based mesh code (Hopkins 2015; Davé et al. 2019; Alonso Asensio et al. 2023).

SIMBA handles radiative cooling and photoionization heating of the gas using the GRACKLE-3.1 library (Smith et al. 2017), including metal cooling and non-equilibrium evolution of primordial elements. The adiabatic and radiative terms are evolved together during a cooling sub-time-step which results in a more accurate and stable thermal evolution, particularly in the stiff regions of the cooling curve (Smith et al. 2017; Davé et al. 2019). This model also includes self-shielding self-consistently during the simulation, based on the Rahmati et al. (2013)'s prescription in which the ionizing background strength is attenuated depending on gas density. A spatially uniform ionizing background is assumed as specified by Haardt & Madau (2012) but modified for self-shielding (Davé et al. 2019).

Star formation in SIMBA-C is modelled using a H_2-based SFR, where the H_2 fraction is computed based on the subgrid model of Krumholz & Gnedin (2011) based on the metallicity and local column density of H_2. The SFR is given by the H_2 density, and the dynamical time is scaled with the efficiency of star formation parameter ϵ_* (Kennicutt 1998):

$$\mathrm{SFR} = \frac{\epsilon_* \rho_{\mathrm{H_2}}}{t_{\mathrm{dyn}}}, \ \epsilon_* = 0.026. \quad (1)$$

Compared to SIMBA, the only change in SIMBA-C is that we use the updated value for ϵ_* from Pokhrel et al. (2021), rather than 0.02 as in Davé et al. (2019). This has no noticeable effect on our results.

SIMBA's chemical enrichment model follows Oppenheimer & Davé (2006) and tracks 11 elements (H, He, C, N, O, Ne, Mg, Si, S, Ca, and Fe) during the simulation, with enrichment tracked from Type II SNe, Type Ia SNe, and asymptotic giant branch (AGB) stars. This uses Nomoto et al. (2006) for SNII yields, Iwamoto et al. (1999) for SNIa yields, and includes AGB star enrichment; see Oppenheimer & Davé (2006) for more details. Type Ia SNe and AGB wind heating are included, along with ISM pressurization at a minimum level to

[2]The interaction of these processes has been extensively studied using observations (Ceverino & Klypin 2009; Smith et al. 2009; Piontek & Steinmetz 2011; Hopkins, Quataert & Murray 2012; Hirschmann, De Lucia & Fontanot 2016; Romano et al. 2019; Lagos et al. 2022 and references therein).

resolve the Jeans mass in star-forming gas as described in Davé et al. (2016). This module is now completely different in SIMBA-C, as we describe in detail in Section 2.2.

SIMBA-C, like SIMBA, models for star formation-driven galactic winds employ decoupled two-phase winds, with a mass loading factor as a function of stellar mass based on particle tracking results from the Feedback in Realistic Environments (FIRE) simulations by Anglés-Alcázar et al. (2017b). SIMBA uses the on-the-fly approximated friends-of-friends (FOF) finder applied to stars and dense gas as described in Davé et al. (2016) to compute galaxy properties such stellar mass, as well as circular velocities using a scaling based on the baryonic Tully–Fisher relation used to set the wind ejection speed. While the mass loading scaling is unchanged, SIMBA-C differs from SIMBA in the velocity scaling, whose normalization has been lowered from the original value of 1.6 to 0.85; the latter value used in SIMBA-C matches the median value predicted by Muratov et al. (2015).

In SIMBA, unlike in SIMBA-C, ejected winds are metal loaded, i.e. when a wind particle is launched, it extracts some metals from nearby particles to represent the local enrichment by the SNe driving the wind. The metallicity added to the wind particle is given by:

$$\mathrm{d}Z = \frac{f_{\rm SNII} y_{\rm SNII}(Z)}{\mathrm{MAX}(\eta, 1)}, \tag{2}$$

where $f_{\rm SNII} = 0.18$ is the stellar mass fraction lost to SNe (assumed to be instantaneous in SIMBA), $y_{\rm SNII}(Z)$ is the metal-dependent Type II SNe yields for each species, and η is the wind mass loading factor. The metal mass is subtracted from the nearby gas in a kernel-weighted manner. If there are not enough metals in the gas particles nearby, then dZ is appropriately reduced.

In SIMBA, Type Ia SNe and AGB stars also provide energetic feedback to the system but are delayed relative to the time of star formation (Davé et al. 2016). Delayed feedback is energetically subdominant relative to the processes driving the winds. SIMBA follows a concurrent (with Type II SNe) prompt component and a delayed component that emerges from stars after an age of 0.7 Gyr for Type Ia SNe, modelled by Scannapieco & Bildsten (2005). Furthermore, SIMBA adds feedback energy from AGB stars to the surrounding gas, based on the model of Conroy, van Dokkum & Kravtsov (2015), in which AGB stellar winds are assumed to be thermalized with ambient gas (Davé et al. 2016). This module is now completely different in SIMBA-C, as we describe in detail in Section 2.2.

SIMBA-C also includes black hole physics models, mostly following SIMBA with some updates. In the original code, black holes are seeded into galaxies not already containing black holes whose stellar mass exceeds $M_* \gtrsim 5 \times 10^9\,\mathrm{M}_\odot$. In SIMBA-C, we instead seed black holes when the galaxy is initially resolved ($M_* \gtrsim 6 \times 10^8\,\mathrm{M}_\odot$), but we suppress black hole accretion exponentially with a factor $\exp(-M_{\rm BH}/10^6\,\mathrm{M}_\odot)$, in order to roughly mimic the behaviour of star formation in dwarf galaxies suppressing black hole growth as described in Anglés-Alcázar et al. (2017b); Hopkins et al. (2022). This change alleviates the 'pile-up' of galaxies seen in SIMBA's stellar mass function just above the M_* where black holes are seeded, owing to a sudden onset of black hole feedback retarding growth; this will be shown for SIMBA-C in Section 3.1 At simulation time, both a dynamical mass and a physical black hole mass are tracked. The dynamical mass is inherited from the parent star particle (effectively the gas mass resolution). The physical mass is set to $M_{\rm BH,seed} = 10^4\,\mathrm{M}_\odot\,h^{-1}$ and allowed to grow via gas accretion.

For black hole growth, SIMBA-C continues to use SIMBA's two-mode accretion model, namely the torque-limited accretion mode presented in Anglés-Alcázar et al. (2017a) for the cold gas, while using Bondi–Hoyle–Lyttleton accretion for the hot gas as the second mode. The total large-scale accretion rate onto each black hole is given as the sum of the two modes, taking into account the conversion of matter into radiation:

$$\dot{M}_{\rm BH} = (1-\eta) \times \left(\dot{M}_{\rm Torque} + \dot{M}_{\rm Bondi}\right), \tag{3}$$

where $\eta = 0.1$ is the radiative efficiency (Yu & Tremaine 2002). $\dot{M}_{\rm Torque}$ follows the prescription discussed in Hopkins & Quataert (2011), Anglés-Alcázar et al. (2017a), and Davé et al. (2019), while the $\dot{M}_{\rm Bondi}$ follows the standard prescription discussed in Bondi (1952):

$$\begin{aligned}\dot{M}_{\rm Torque} &\equiv \epsilon_T f_d^{5/2} \left(\frac{M_{\rm BH}}{10^8\,\mathrm{M}_\odot}\right)^{1/6} \left(\frac{M_{\rm enc}(R_0)}{10^9\,\mathrm{M}_\odot}\right) \\ &\quad \times \left(\frac{R_0}{100\,\mathrm{pc}}\right)^{-3/2} \left(1 + \frac{f_0}{f_{\rm gas}}\right)^{-1} \mathrm{M}_\odot\,\mathrm{yr}^{-1}, \\ \dot{M}_{\rm Bondi} &= \frac{4\pi G^2 M_{\rm BH}^2 \rho}{c_{\rm s}^3}. \end{aligned} \tag{4}$$

Like SIMBA, SIMBA-C limits the torque mode accretion rate to three times the Eddington accretion rate and the Bondi mode to the Eddington rate.

The accretion energy is used to drive the black hole feedback that quenches galaxies. In SIMBA-C this is done by using a kinetic subgrid model for black hole feedback, along with X-ray energy feedback (Davé et al. 2019). The reason for this comes from the observed dichotomy in black hole growth modes that is reflected in their outflow characteristics (e.g. Benson & Babul 2009; Heckman & Best 2014): A 'radiative mode' at high Eddington ratios ($f_{\rm Edd} \equiv \dot{M}_{\rm BH}/\dot{M}_{\rm Edd} \gtrsim$ few per cent), in which AGNs are seen to drive multi-phase winds at velocities of $\sim 1000\,\mathrm{km\,s^{-1}}$ that include molecular and warm ionized gas (e.g. Sturm et al. 2011; Perna et al. 2017); and a 'jet mode' at low Eddington ratios, where AGNs, mostly drive hot gas in collimated jets that in clusters are seen to inflate supervirial temperature bubbles in surrounding gas (e.g. McNamara & Nulsen 2007; Jetha et al. 2008; Fabian 2012). According to Best & Heckman (2012); Davé et al. (2019), this dichotomy also appears in radio jet activity ('high excitation' versus 'low excitation' radio galaxies) above and below roughly a per cent of the Eddington rate, with the former tending to be found in lower mass, bluer host galaxies and the latter in massive early-types (see Thomas et al. 2021).

SIMBA-C's AGN feedback model is designed to directly mimic the energy injection into large-scale surrounding gas from these two modes, using purely bipolar feedback in the angular momentum direction of the black hole accretion radius (i.e. 256 nearest neighbours), with velocities and temperature taken as much as possible from AGN outflow observations. In SIMBA-C, the velocity kick is given by

$$v_w = 500 + 500 \log_{10} \left(\frac{M_{\rm BH}}{10^6\,\mathrm{M}_\odot}\right)^{1/3} + v_{\rm jet}, \tag{5}$$

where $v_{\rm jet}$ is only included if the Eddington ratio $f_{\rm Edd} < 0.2$, and is given by:

$$v_{\rm jet} = 7000 \log_{10} \frac{0.2}{MAX(f_{\rm Edd}, 0.02)}\ \mathrm{km\,s^{-1}}. \tag{6}$$

This differs from SIMBA only in the jet cap term, which was just $7000\,\mathrm{km\,s^{-1}}$, but now is roughly scaled with the halo escape velocity, so this cap scales up in the ability of jets to escape from halos in the group and cluster regime. This was originally proposed in the Three

Hundred Cluster Zoom (Cui et al. 2022). However, it has a negligible effect on the mass scales covered in this work. .

Another change from SIMBA is the mass scale above which jets are allowed. In SIMBA, this was $4 \times 10^7\,M_\odot - 6 \times 10^7\,M_\odot$, while in SIMBA-C it is $7 \times 10^7\,M_\odot - 1 \times 10^8\,M_\odot$. Moreover, in SIMBA this was implemented as a random value with a probability scaling from $0 \rightarrow 1$ over that mass range, while in SIMBA-C each black hole particle is effectively assigned its own jet onset mass which it retains throughout the run.

To model the ejection as purely bipolar, the ejected gas elements are ejected in a positive and negative direction parallel to the angular momentum vector of the inner disc, typically the nearest 256 gas particle neighbouring the black hole. SIMBA also included an energy input into the surrounding gas from X-rays of the accretion disc (Davé et al. 2019) as motivated by Choi et al. (2012) assuming a radiative efficiency of $\eta = 0.1$. SIMBA applies this heating only when the jet mode is active.

The above-described changes in SIMBA-C are a result of trial-and-error calibration, likely driven by the lower amount of metals produced by the Chem5 model than by SIMBA's instantaneous enrichment model. For example, this means that the metal cooling is less efficient, which motivates a later onset of jet feedback. The calibration is still done purely on stellar and black hole quantities, i.e. the stellar mass function evolution and the black hole mass-stellar mass relation, as was the case in SIMBA; no direct tuning was done based on the chemical enrichment model.[3]

2.2 The Chem5 chemical enrichment model

The primary new feature of SIMBA-C is the introduction of the new chemical enrichment model which we call Chem5. Chem5 is the 'version-5' of a self-consistent 3D chemodynamical enrichment model developed by Kobayashi (2004); Kobayashi et al. (2007); Taylor & Kobayashi (2014),[4] with continued improvements by Kobayashi & Nakasato (2011) and Kobayashi, Leung & Nomoto (2020a); Kobayashi, Karakas & Lugaro (2020b). Furthermore, the Chem5 model has also been used in other studies such as Vincenzo & Kobayashi (2018b) and Ibrahim & Kobayashi (2023). The model tracks all the elements from Hydrogen (H) to Germanium (Ge), thereby expanding on the existing list of elements within SIMBA. This model also introduces various physical processes associated with the formation and evolution of stellar systems. The physical processes that are included in the Chem5 model include chemical enrichment and energy feedback from core-collapse SNe (incl. hypernovae and 'failed' supernovae), from Type Ia SNe, and from stellar winds for stars of all masses including AGB and super-AGB stars. We refer the reader to Kobayashi et al. (2020a, b) for a full description of each of these processes, including the yield table for each enrichment channel. Here, we will only be summarizing the main concepts behind each process.

[3]The metallicity results were used as an indicator to calibrate the SFR. This was needed since the number of stars produced was lower than in SIMBA due to fewer amounts of metals predicted by the Chem5 model, which led to a weaker metal cooling function, resulting in a stronger feedback system, creating fewer stars. Therefore, the feedback system was reconfigured (see Section 2.2).

[4]By self-consistent, we mean tracking the metal return following a detailed stellar evolution model with mass- and metal-dependent yields.

2.2.1 Stellar winds

As a star evolves, two components are taken into account: (i) The metals that are processed through nucleosynthesis at the formation site to form new metals. (ii) When a star is dying, stellar winds return a fraction or all of their unprocessed metals (locked-up in the star's envelope since its formation) to the ISM. According to Kobayashi et al. (2020b), both components are included in the same nucleosynthesis table for AGB stars, while only processed metal yields are included in the SNe yields (see equation 9 in Kobayashi, Tsujimoto & Nomoto 2000). The amount of mass containing these metals that is ejected by the stellar winds in the Chem5 model is given as:

$$M_{\rm wind} = M_{\rm init} - M_{\rm remnant} - \sum_i p_{z_i m}, \tag{7}$$

where $M_{\rm init}$ is the initial mass of the star, $M_{\rm remnant}$ is the mass of the left-over remnant (e.g. black hole, neutron star, or white dwarf), while $p_{z_i m}$ is the nucleosynthesis yield of an element.

2.2.2 Asymptotic giant branch stars

Depending on the metallicity, all stars with masses between $\sim$0.9 and $8\,M_\odot$ pass through the thermally pulsing AGB phase (Kobayashi et al. 2020b). This phase, in particular, can lead to the enrichment of ^{12}C on the surface of a star if the convective envelope is hot enough to sustain proton-capture nucleosynthesis. This happens because the He-burning shell becomes unstable during this phase, leading to processed metals from nuclear reactions in the core mixing with the envelope. Furthermore, this newly created ^{12}C can then be converted into ^{14}N by means of the CNO cycle (a *primary* process). Similarly ^{23}Na and Al can be created through the NeNa and MgAl cycles, respectively. Through stellar winds, these metals can be ejected from the star over its lifetime.

The ejected masses of each element are added to the yield tables. The new yields are calculated as the difference between the amount of the species in the winds and the initial amount in the envelope of the progenitor star. The initial abundances are set to the scaled proto-solar abundances calculated by Asplund et al. (2009). Therefore, $p_{z_i m}$ could become negative, especially for H. It is therefore important to track the unprocessed metals to conserve mass.

2.2.3 Super asymptotic giant branch stars

The fate of high-mass stars, specifically stars with initial masses between 8 and $10\,M_\odot$ (at $Z = 0.02$), is still uncertain (Doherty et al. 2017; Kobayashi et al. 2020b). It is accepted that the upper mass limit of the AGB stars, $M_{{\rm up},C}$, is defined as the minimum mass for the ignition of C. A hybrid C+O+Ne white dwarf (WD) can be formed when a star has a mass above this upper limit, due to neutrino cooling and contraction leading to ignition of C off-centre. This then propagates to the centre, but not completely all the way. However, below the upper mass limit, two different outcomes can occur. If the mass is $\lesssim 9\,M_\odot$, the C ignition moves all the way to the centre, while it will undergo central C ignition if the mass is $\gtrsim 9\,M_\odot$. Both of these outcomes will result in a degenerate O+Ne+Mg core, which could lead to an O+Ne+Mg WD, if the outer shell is lost through stellar winds.

From this we can extract another upper mass limit, specifically for Ne: $M_{\rm up,Ne} \sim 9\,M_\odot$. This in turn will lead to a new off-centre ignition, this time for Ne. This will then result in WDs of O+Ne+Mg or O+Ne+Fe. These processes and nucleosynthesis yields up to Ni

have been included in the Chem5 tables. They were collected from Doherty et al. (2014a, b), and are scaled to the solar abundances from Grevesse, Noels & Sauval (1996).

2.2.4 *Type Ia supernovae*

The majority (more than 75 per cent Kobayashi et al. 2020a) of SNe Ia are believed to have occurred due to Chandrasekhar mass WDs. The Chem5 model's nucleosynthesis yields for Type Ia are based on this fact. Therefore, because of the model's reliance on this, understanding of the evolution of accreting C+O WDs towards this mass is important. Kobayashi et al. (2020a) noted that two scenarios have been proposed: (i) A double-degenerate (merging of two WDs). (ii) A single degenerate, where the WD's mass grows via accreting mass from a binary companion, which is rich in H-matter. The Chem5 model follows the latter scenario. The lifetime distribution function of the SNe Ia for this scenario in the Chem5 model is calculated using:

$$R_{\rm Ia} = b \int_{\max[m_{\rm p,l}, m_{\rm t}]}^{m_{\rm p,u}} \frac{1}{m}\phi(m){\rm d}m \times \int_{\max[m_{\rm d,l}, m_{\rm t}]}^{m_{\rm d,u}} \frac{1}{m}\psi(t-\tau_{\rm m})\phi_{\rm d}(m){\rm d}m, \quad (8)$$

where these integrals are calculated separately for the primary and secondary stars (m_p and m_d; Kobayashi & Nomoto 2009), taking into account the metallicity dependence of the WD winds (Kobayashi et al. 1998) and the mass stripping effect on the binary companion stars (Kobayashi & Nomoto 2009).

A double peak is obtained, since the lifetime of the SNe Ia is determined by the companion stars. These peaks occur between: (i) $\sim 0.1 - 1$ Gyr for main-sequence-WD systems, dominating in star-forming galaxies. (ii) $\sim 1 - 20$ Gyr for re-giant-WD systems – dominating in early-type galaxies (Kobayashi & Nomoto 2009; Kobayashi et al. 2020a). Furthermore, for the yields themselves, they are calculated with delayed detonations in Chandrasekhar-mass C+O WDs as a function of metallicity with solar-scaled initial compositions (Kobayashi et al. 2020a).

It must be noted that with recent observations of SNe Ia in galaxies and clusters, an empirical approach delay time distribution (DTD – see Maoz & Graur 2017) rather than an analytical approach is often used to determine the SNe Ia rates in galaxy simulations. However, as shown in Kobayashi et al. (2020a, 2023), this approach does not reproduce the elemental abundance observations in the Milky Way. The analytical formula can reproduce not only the elemental abundance observations but also the DTD. It is based on progenitor models, including the metallicity dependence. With this formula, it is also possible to include sub-Chandrasekhar-mass explosions of SNe Ia in the future.

2.2.5 *Core-collapse supernovae*

According to Kobayashi et al. (2020b), the Chem5 model only uses nucleosynthesis yields from 1D calculations as presented in Kobayashi et al. (2006); Kobayashi, Karakas & Umeda (2011) for core-collapse SNe. The yields for massive star SNe have been provided by three different groups (Woosley & Weaver 1995; Nomoto et al. 1997; Limongi, Chieffi & Bonifacio 2003) and are constantly being updated. The reason for this is that the explosion mechanism is still uncertain for Type II, Ib, and Ic SNe. Furthermore, the Fe mass ejected by various different multidimensional simulations is not as large as observed, such as in Marek & Janka (2009).

Some of the uncertainties in these yields are the reaction rates, mixing in stellar interiors, rotationally induced mixing processes, mass-loss via stellar winds, and the formation of remnants (see §3.6 of Kobayashi et al. 2020b). Different solutions have been modelled to solve these uncertainties, such as the mixing fall-back model introduced by Umeda & Nomoto (2002), to mimic this multidimensional simulation phenomenon in 1D calculations. The Chem5 model follows the approach where the quantities, such as the ejected explosion energy and ^{56}Ni mass[5] are determined independently through light curve and spectral fitting of an individual SN (Kobayashi et al. 2006; Nomoto, Kobayashi & Tominaga 2013; Kobayashi et al. 2020b), thereby constraining them with observations. This method was introduced in Kobayashi et al. (2006).

As a result, hypernovae (HNe; Kobayashi et al. 2020b) are produced by the Chem5 model. HNe are core-collapse SNe with masses between $M \geq 20\,{\rm M}_\odot$ and have explosion energies greater than 10 × that of a regular SN. They also produce more Fe and α elements. As for the nucleosynthesis yields for SNe II and HNe, they are provided separately as a function of the progenitor mass and metallicity. The fraction of HNe at a given time is uncertain and is set to a maximum of $\epsilon_{\rm HN} = 0.5$ with declining values based on the metallicity dependence introduced in Kobayashi & Nakasato (2011). It is important to note that the Chem5 model does not include stellar rotation which is believed to be necessary to explain the observed N/O–O/H relation (Frischknecht et al. 2016; Limongi & Chieffi 2018). According to Vincenzo & Kobayashi (2018a), by using a more self-consistent cosmological simulation, the observed relation can be reproduced with inhomogeneous enrichment from AGB stars.

2.2.6 *'Failed' supernovae*

The upper limit of SNe II is not well known, because no progenitor stars are found at the locations of nearby SNe II with initial masses $M > 30\,{\rm M}_\odot$. This has raised the question of whether massive SNe II can explode.[6] To take this into account, Kobayashi et al. (2020b) introduced a new set of nucleosynthesis yields, called 'failed' SNe, at the massive end of SNe II while keeping the contributions from HNe.

For the yields of 'failed' SNe, it is assumed that all CO cores fall onto black holes and are not ejected into the ISM in multidimensional time-scales, since it is not long enough to follow this process. Therefore, the upper mass limit is treated as a free parameter while it stays the same for HNe. It is important to note that 'failed' SNe are not the same as 'faint' SNe, which are not included in the Chem5 model.

2.3 Implementation

In this section, we detail the integration of the Chem5 chemical enrichment model and its various physical enrichment processes into SIMBA.

First, we send the information for every single star particle to the Chem5 model at the beginning of every time-step. The Chem5 model treats star particles as an evolving stellar population that can eject thermal energy, mass, and heavy elements based on the initial and current properties of the stellar particle (Kobayashi 2004). The

[5]^{56}Ni mass decays to ^{56}Fe and forms most of the ejected Fe mass.

[6]Multidimensional simulations also seem to find it difficult to explode stars with $\gtrsim 25\,{\rm M}_\odot$ with the neutrino mechanism (Janka 2012).

contributions from all the stellar feedback channels within a given time-step are determined.

Two things must be noted: First, since a star particle represents an entire stellar population, it can undergo multiple events. If multiple events occur simultaneously, for instance, a SNe Ia and a AGB stellar feedback event, then the Chem5 model adds the results for the two events together and returns a value for each of the three ejected variables, namely mass, metals, and energy. We distribute these ejecta to neighbouring gas particles in a kernel-weighted fashion. In SIMBA, it gets distributed to the nearest 64 neighbouring gas particles. Specifically, for the injection of the metals, we use:

$$Z_{\mathrm{j,k}} = \left(1 - \frac{\mathrm{d}M_{\mathrm{ej,in}}}{M_{\mathrm{j}}}\right) Z_{\mathrm{j,k}} + \frac{\mathrm{d}M_{\mathrm{ej,in}}}{M_{\mathrm{j}}} Z_{\mathrm{ej,k}}, \tag{9}$$

where $Z_{\mathrm{j,\,k}}$ is the metallicity of the neighbouring gas particle, $\mathrm{d}M_{\mathrm{ej,\,in}}$ is the kernel-weighted ejected mass fraction, M_{j} is the gas particle's mass, and $Z_{\mathrm{ej,\,k}}$ the ejecta metallicity for the star particle, while k represents each element in the sample. After the distribution of these ejecta, $\mathrm{d}M_{\mathrm{ej,\,in}}$ is then removed from the star particle to ensure that the conservation of the metal mass/energy is followed.

It is important to note that the energy ejection from SNe Type II in the Chem5 model is not being distributed, since it is already being effectively employed by the star formation-driven wind model within SIMBA. The parameter $f_{\mathrm{SNII}} = 0.18$ for SIMBA, is set to zero in SIMBA-C since this parameter represented an instantaneous mass-loss due to Type II SNe within the first $\sim$ 30 Myr, but now we are removing this instantaneous recycling approximation.

Although the metal content influences metal cooling, we did not make any changes to the cooling function within GRACKLE-3.1, and therefore the cooling occurs exactly the same way as in SIMBA.

2.4 Dust integration

We are not including the dust model from SIMBA as presented in Davé et al. (2019) in this update. The reason behind this is that the dust model influences the outcome of the individual elemental abundance, and for the purpose of this study, we want to test the Chem5 model's impact on the SIMBA simulation. The dust model can run concurrently with the new model, but it has not been tested or calibrated to the new elemental abundances. We leave this to future work.

2.5 Chabrier IMF

Since we are working with star particles that represent an entire stellar population, we need to adopt an initial mass function (IMF) that describes the stellar mass distribution of this population. For consistency between SIMBA and the Chem5 model, we use the Chabrier IMF (Chabrier 2003), unlike Kobayashi et al. (2020b). Specifically, we use a renormalized version of the Chabrier equation given by Romano et al. (2005). The newly introduced Chabrier IMF is given as:

$$\varphi_{\mathrm{Chabrier}}(m) = \begin{cases} A_{\mathrm{Chabrier}} \mathrm{e}^{(\log m - \log m_{\mathrm{c}})^2/2\sigma^2} & \text{if } m \leq 1\ \mathrm{M}_{\odot}, \\ B_{\mathrm{Chabrier}} m^{-1.3} & \text{if } m > 1\ \mathrm{M}_{\odot}; \end{cases} \tag{10}$$

with $A_{\mathrm{Chabrier}} \simeq 0.79$ and $B_{\mathrm{Chabrier}} \simeq 0.22$ for our normalization constants. Furthermore, we also use $m_{\mathrm{c}} = 0.079\,\mathrm{M}_{\odot}$ and $\sigma = 0.69$ as in Romano et al. (2005).

2.6 Motivating the parameter changes from SIMBA

Our initial attempt to incorporate the CHEM5 model into SIMBA, without recalibrating, significantly underproduced metals compared to the observational results in Yates et al. (2021) at all redshifts. We found that the metal cooling rates at low redshift are so inefficient that the stellar feedback model overheats all of the gas – leading to fewer stars being produced, in turn creating fewer metals. Therefore, we found that it is essential to recalibrate SIMBA.

First, we found that we must increase the minimum black hole jet mass threshold, which leads to fewer stellar feedback events occurring. Recall that SIMBA has a black hole mass range where the jet begins to operate, $M_{\mathrm{min,\,jet}}$, and slowly ramps up to maximum power at $M_{\mathrm{max,\,jet}}$. The mass range was kept within the same order of magnitude. Specifically, we changed this black hole jet activation parameter from $4 \times 10^7\,\mathrm{M}_{\odot} - 6 \times 10^7\,\mathrm{M}_{\odot}$ to $7 \times 10^7\,\mathrm{M}_{\odot} - 1 \times 10^8\,\mathrm{M}_{\odot}$. Our changes increased the SFRs of the simulated galaxies, which in turn increased the number of metals in the system.

However, our changes negatively affected the L^* region of the $z = 0$ galaxy stellar mass function (GSMF). We found that we needed to further recalibrate SIMBA by changing the wind velocity scaling. Recall that SIMBA stellar feedback relies on the results of Muratov et al. (2015) for wind mass loading η and wind velocity v_{w}. In SIMBA, the wind velocity followed:

$$v_{\mathrm{wind}} = 1.6 \left(\frac{v_{\mathrm{circ}}}{200\,\mathrm{km\,s^{-1}}}\right)^{0.12} + v_{\mathrm{corr}}, \tag{11}$$

where v_{circ} is the circular velocity of the galaxy, and v_{corr} is a correction term for the wind launch location compared to Muratov et al. (2015). The normalization, $a = 1.6$, of this equation was set much higher in SIMBA compared to $a = 0.85$ in Muratov et al. (2015). By lowering this value from the default $a = 1.6$ SIMBA value to the $a = 0.85$ originally found in Muratov et al. (2015), we improved the GSMF and cosmic SFR's history. Specifically, it increased $z = 2$ SFR, while lowering it at $z = 0$, resulting in a better match with the observations of Madau & Dickinson (2014). All of the above-mentioned parameter chances are shown in Table 1.

2.7 Runs and analysis

In this paper, we have two simulations: (i) The original SIMBA volume with the previous chemical enrichment module as a control, as well (ii) Our SIMBA-C code including Chem5.[7] Both runs consist of volumes of side length $50\,\mathrm{Mpc\,h^{-1}}$ with 512^3 gas and 512^3 dark matter particles down to $z = 0$. Given that we are most concerned with enrichment in star-forming galaxies in this paper, the volume is sufficient to get a good sample of such objects.

Both runs begin at $z = 249$ and follow a Planck Collaboration VI (2018) ΛCDM cosmology of $\Omega_m = 0.3$, $\Omega_\Lambda = 0.7$, $\Omega_b = 0.048$, and $H_0 = 68\,\mathrm{km\,s^{-1}\,Mpc^{-1}}$. We analyse the simulation outputs using an FOF galaxy finder to identify galaxies, assuming a spatial linking length of 0.0056 times the mean interparticle spacing. Galaxies and haloes are cross-matched in post-processing using Caesar, a yt-based package.[8] Galaxy finding is applied to all stars and black holes, as well as to all gas elements with a density above the minimum SF threshold density $n_H > 0.13\,\mathrm{H\,atoms\,cm^{-3}}$. Black holes are assigned

[7]The MUSIC-created initial conditions are the same for both simulations.
[8]Caesar documentation can be found at https://caesar.readthedocs.io/en/latest/

Table 1. Summary of all the differences between SIMBA (discussed in Section 2.1) and SIMBA-C (discussed in Section 2.2), based on all the implementation and integration changes that were necessary (Section 2.3 to Section 2.5), and module/parameter changes due to calibrations (Section 2.6 and Section 3.2).

Changed ingredients	**SIMBA**	**SIMBA-C**
Chemical enrichment model	Instantaneous recycling approximation	Chem5 evolving chemical enrichment
Stellar feedback types	Stellar winds, SNe Ia, AGB, SNe II	Stellar winds, SNe Ia, two AGBs, SNe II, HNe, 'Failed SNe'
Elements	H, He, C, N, O, Ne, Mg, Si, S, Ca, and Fe	H→Ge
Dust	Included	Excluded
IMF	Chabrier	Chabrier ∼ changed from Kroupa
Wind velocity scaling	$\alpha = 1.6$	$\alpha = 0.85$ (now matching Muratov et al. 2015)
Black hole jet mass activation min	4×10^7 M$_\odot$	7×10^7 M$_\odot$
Black hole jet mass activation max	6×10^7 M$_\odot$	1×10^8 M$_\odot$
SNe II mass fraction	$f_{\rm SN\,II} = 0.18$	$f_{\rm SNII} = 0$

to galaxies to which they are most gravitationally bound. The central black hole is considered the most massive black hole in the galaxy.

3 RESULTS

We first investigate the impact of the Chem5 model on global galaxy properties by comparing SIMBA-C with SIMBA. The purpose of these comparisons is to identify whether the new model is able to reproduce the accuracy of galaxy populations that SIMBA obtained in Davé et al. (2019), and secondly to determine whether SIMBA-C has improved on SIMBA's minor discrepancies compared to observations.

3.1 Stellar properties

In this section, we investigate the global scaling relationships and galaxy distributions through the GSMF, the black hole stellar mass relation, and the quenched fraction of the galaxy population. We note that these properties have been tuned to reproduce observations in SIMBA, but we did not re-tune them for SIMBA-C.

The GSMF characterizes the efficiency with which haloes can convert baryons to stars (Davé et al. 2011, 2019). Since we are comparing the SIMBA model and the new SIMBA-C model, we use the same observational data as Davé et al. (2016) for comparison.

In Fig. 1, we show the evolution of the GSMF at $z = \{6, 4, 3, 2, 1, 0\}$ for the SIMBA-C model. At $z = 6$ and $z = 4$, we used observational data based on the Cosmic Assembly Near-infrared Deep Extragalactic Legacy Survey (CANDELS) from Song et al. (2016). For $z = \{3, 2, 1\}$, we used data from Tomczak et al. (2014) – a combination of the CANDELS and the FourStar Galaxy Evolution Survey (zFOURGE) data – as well as the results of Muzzin et al. (2013) from the Ultra Deep Survey with the Visible and Infrared Survey Telescope (UltraVISTA) within the Cosmic Evolution Survey (COSMOS). Lastly, for $z = 0$, we use both the results of Bernardi et al. (2017) and Baldry et al. (2012) (part of the Galaxy and Mass Assembly – GAMA project).

Similarly to Davé et al. (2019), we also show the subsets of the mass functions based on the SFR in Fig. 1. These are shown as a blue line, representing the 'blue' galaxies (star-forming galaxies), and a red line, representing the red and dead 'quenched' galaxies. We use the specific SFR to distinguish between the two, namely the specific SFR (sSFR $= 10^{-1.8+0.3z}$ Gyr^{-1}). The combination of these two populations is our total stellar mass function, of which the median is plotted with the green line, and the green band represents the 1σ cosmic variance uncertainties on this calculation obtained by taking the variance over the GSMF in eight simulation octants.

From Fig. 1, it is clear that on average SIMBA-C agrees quite well with the observed GSMF at all redshifts. For the higher redshift ranges, the blue star-forming galaxies follow the total mass function nearly identically, meaning that the contribution from quenched galaxies between $3 \leq z \leq 6$ is almost non-existent. This remains an issue with the SIMBA family of models, that they may not produce sufficient numbers of quenched massive galaxies at high redshifts (Sherman et al. 2020). Furthermore, it is also clear that no massive star-forming galaxies are produced at these higher redshifts. This is related to the volume of the simulation box. At this volume, simulations produce very few massive galaxies, therefore it is improbable to form massive galaxies (star-forming or quenched) at earlier redshifts.

From $z = 2$ to the present day, quenched galaxies start to contribute more, especially at higher masses ($M_* \gtrsim 10^{11}$ M$_\odot$). This is quite evident for the blue star-forming galaxies at $z = 1$ and $z = 0$, where they drop steeply at $M_* \sim 10^{11.4}$ M$_\odot$. The switch between high-redshift GSMF being dominated by star-forming galaxies, while quenched galaxies start to dominate at lower redshifts, is as expected, since galaxies start to quench due to AGN feedback from massive black holes combined with dropping gas accretion rates, and is broadly inferred from observations (e.g. Faber et al. 2007).

Fig. 2 shows a comparison of the stellar mass function at $z = 0$ between the SIMBA (red line) and SIMBA-C (blue band) results, compared to several recent observational determinations. Fig. 2 clearly shows that the new model is in better agreement with the observational data.

Two areas stand out. The first is the evident improvement at $M_* \sim 10^{9.7}$ M$_\odot$, where SIMBA shows a bump, while SIMBA-C shows no particular feature at that mass scale, which is more consistent with observations. Secondly, we see that in the mass range $10^{10.1}$ M$_\odot \leq M_* \leq 10^{11.5}$ M$_\odot$, on average, SIMBA predicts a GSMF value that is ~ 0.3 dex lower than the observations. This was also seen in Davé et al. (2019), where SIMBA undercuts the GSMF around the knee, an issue that is problematic for many galaxy formation models. SIMBA-C shows a great improvement over SIMBA in this regard, with all observational results within the error, as well as the median of the simulation following the trend of the data almost identically, with a slight underestimate by ~ 0.1 dex for the lower mass end. This increase is the result of the change in the velocity scaling parameter (from 1.6 to 0.85 as described in Section 2.3) necessary for the SFR due to the metal cooling function being inefficient. This change to the velocity scaling parameter is now more consistent with the result found in Muratov et al. (2015) using the FIRE simulations. Since SIMBA as a whole is calibrated and constrained to $z = 0$, this is a valuable improvement, particularly for galaxies of the Milky Way size.

Finally, we check that SIMBA-C is still quenching massive galaxies at $z = 0$ in accordance with observations. We show a histogram of the sSFR as a function of the mass of the galaxies at

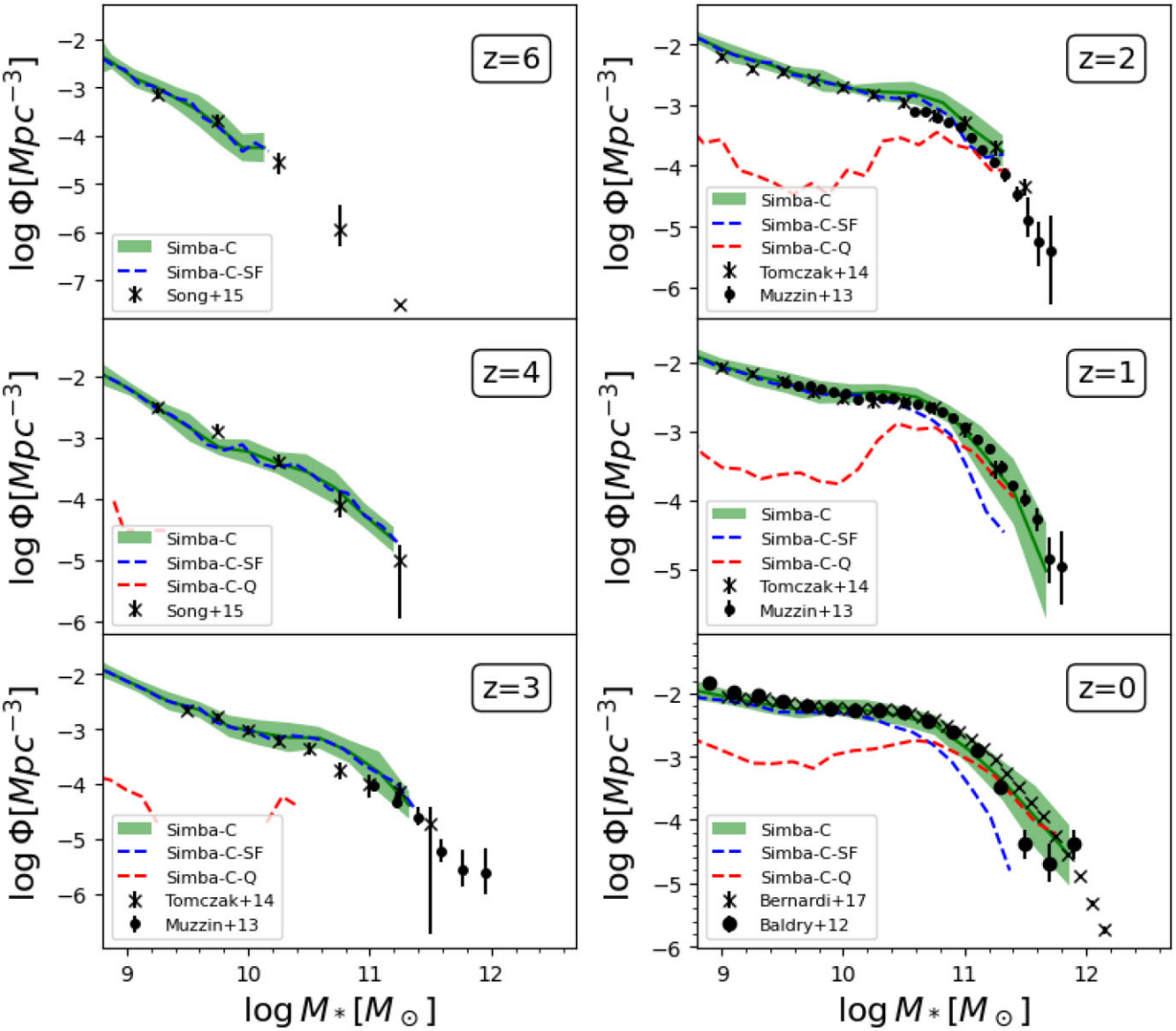

Figure 1. The evolution of the stellar mass function for the SIMBA-C simulation from $z = 6 \rightarrow 0$, compared to different observations from Song et al. (2016) for $z = 6$ and $z = 4$, Muzzin et al. (2013); Tomczak et al. (2014) for $z = 3$, 2, 1, and Baldry et al. (2012); Bernardi et al. (2017) for $z = 1$ and $z = 0$. The red and blue dashed lines represent the median of the galaxy's sSFR and are divided into the two populations at $= 10^{-1.8+0.3z}$ Gyr^{-1}, while the green band shows the combined results of all the star-forming and quenched galaxies within the SIMBA-C simulation.

$z = 0$ in Fig. 3. From the GALEX-SDSS-WISE LEGACY Catalogue (GSWLC)-X2 (Salim, Boquien & Lee 2018), we use the master observations catalogue with the complete set of galaxies, which is different from the deep catalogue (which only uses a subset of the full catalogue) used in Davé et al. (2019); this allows better statistics for massive galaxies, but the results are not significantly different. We binned the galaxies according to their stellar masses as follows: $10^9\,\mathrm{M}_\odot < M_* \leq 10^{10}\,\mathrm{M}_\odot$ (blue lines), $10^{10}\,\mathrm{M}_\odot < M_* \leq 10^{11}\,\mathrm{M}_\odot$ (green), and $M_* > 10^{11}\,\mathrm{M}_\odot$ (red). Similarly to Davé et al. (2019), all sSFR$<10^{-2.5}$ are delegated to the lowest mass bin at that value. The observations are binned similarly and shown using dotted lines with a filled circle marker.

The overall bimodal distribution with a populous main sequence of blue galaxies, a similar number of quenched galaxies, and a dearth of galaxies in the green valley is present in both SIMBA runs, which is broadly consistent with the observations. But there are significant differences in the details, between SIMBA and SIMBA-C.

Looking at each mass bin individually, starting with the lowest mass range, we see a noticeable improvement over SIMBA relative to the observations at the main-sequence peak. SIMBA-C is much closer to the GSWLC-X2 data, although still with a slight offset from the higher sSFR. This is noteworthy, considering the fact that SIMBA was already in good agreement with the low-mass star-forming galaxies.

Another major area of improvement is in the green valley, particularly regarding intermediate mass galaxies (green lines), which dominate the green valley population. In SIMBA, the green valley is not as empty as it should be, as also noted in Davé et al. (2019), which results in less of a bimodal distribution than observed. Conversely, SIMBA-C produces excellent agreement with observations around sSFR$\approx 10^{-1.5} - 10^{-2}$ Gyr^{-1}, showing a clear drop relative to the

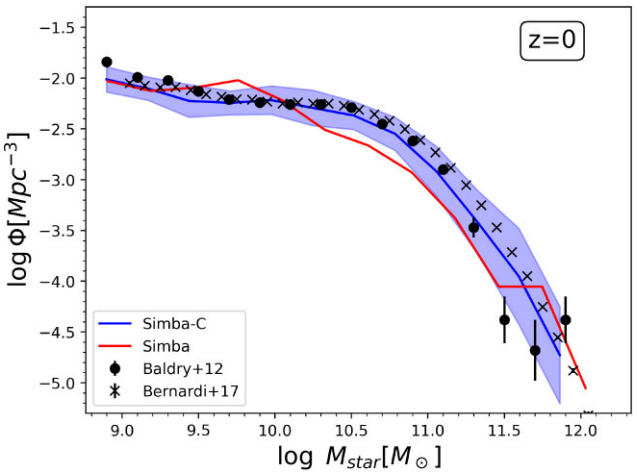

Figure 2. Comparison of the stellar mass function between the SIMBA-C simulation and the published version of SIMBA at $z = 0$, compared to the same observations as in Fig. 1. The SIMBA-C simulation median results (same results as the green band in the last panel of Fig. 1) are shown by the blue line with its spread in the light blue band, while the red line displays the median SIMBA results for comparison.

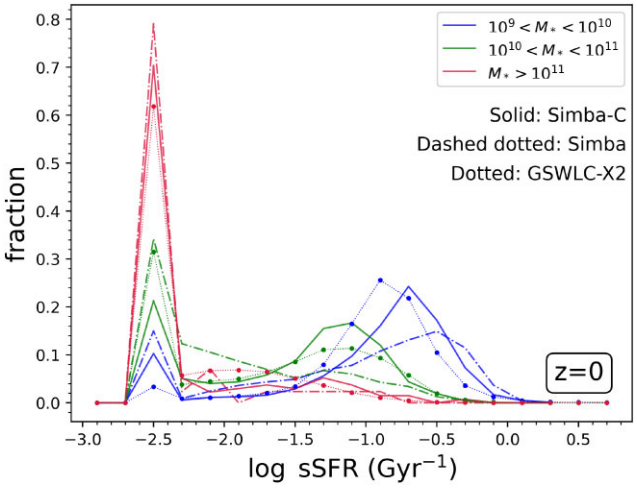

Figure 3. Histogram of sSFR in three bins of stellar mass. The solid lines show the results for SIMBA-C, and the dashed dotted lines show the SIMBA equivalent at $z = 0$. The observations are from the GSWLC-X2 catalogue described in Salim et al. (2018), with redshifts on average between $\sim 0.2 > z \geq 0$ and shown with the dotted lines with a filled circle marker to distinguish them from their simulation counterparts. All galaxies with sSFR$<10^{-2.5}$ are placed in the lowest bin.

populations at higher and lower sSFR within this mass bin. Hence, the impact of the new model appears to cause a more rapid transition of galaxies through the green valley within this key mass range, in better agreement with observations.

In the high mass range, SIMBA-C is also in better agreement with observations. For SIMBA the fraction of quenched high mass galaxies is $\sim$0.80, while for SIMBA-C it is $\sim$0.70, while for observations it is $\approx$0.65. Although we see an improvement over SIMBA, SIMBA-C is still overproducing massive quenched galaxies relative to massive star-forming galaxies.

We also test the black hole mass to stellar mass ratio to see the impact of updating SIMBA's black hole seeding and feedback modules. Fig. 4 shows the comparison between the median SIMBA simulation

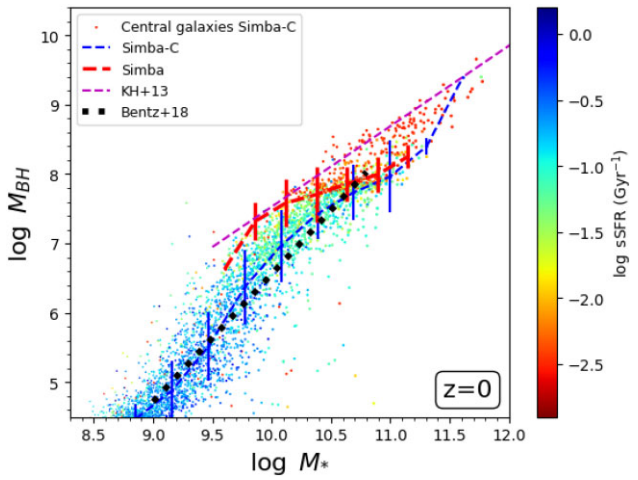

Figure 4. Comparison of the $M_{\rm BH} - M_*$ relation at $z = 0$ between the SIMBA-C simulation and SIMBA, and the observational results from Kormendy & Ho (2013); Bentz & Manne-Nicholas (2018). We also include the central galaxy values from the CAESAR galaxy catalogue for the SIMBA-C simulation, which were used to determine the median $M_{\rm BH} - M_*$ value in its host galaxy and scaled their representing colour to their host galaxy's sSFR. The colour distribution corresponds to the blue being star forming galaxies, while red represents quenched galaxies.

results (red line) and the median SIMBA-C results (blue line) at $z = 0$. We colour-coded the individual central galaxies contributing to the median based on their sSFR from the SIMBA-C model. We also use two sets of observational data, namely Kormendy & Ho (2013) for comparison with the larger redder/quenched galaxies and Bentz & Manne-Nicholas (2018) for the smaller blue/star-forming galaxies.

From Fig. 4, we see that SIMBA-C spans a much larger range in black hole masses and stellar masses of the host galaxies than SIMBA. Specifically, we have more blue star-forming galaxies following very closely the Bentz & Manne-Nicholas (2018) observations, whereas SIMBA has a hard cut-off at $M_* \sim 10^{9.6}$ M$_\odot$. This owes to the earlier black hole seeding in SIMBA-C, and means that in the new version we are able to track black hole growth much earlier. The agreement with the observed slope of Bentz & Manne-Nicholas (2018) is adjusted by choosing the exponential accretion suppression factor. However, SIMBA-C still does not reproduce the large scatter seen in observations at low M_* in this relation (not shown). Meanwhile, at the high M_* end, we also find that our quenched galaxies follow the trend of Kormendy & Ho (2013), albeit somewhat lower; this is not significantly changed from SIMBA. The main take away from this is that the integration of Chem5 model into SIMBA did not negatively change the black hole results, but also allowed tracking of black hole growth in lower mass galaxies.

3.2 Metallicities and abundance ratios

The key change in SIMBA-C is the addition of the new chemical enrichment module. To test this, we now investigate the metallicity content of our simulated galaxies. In this Section, we also discuss our recalibration of the stellar feedback strength through the wind launch velocity scaling.

3.2.1 Mass–metallicity relations

First, we investigate the stellar mass – gas-phase metallicity relation (MZR) and the stellar mass – stellar metallicity relation. In Fig. 5,

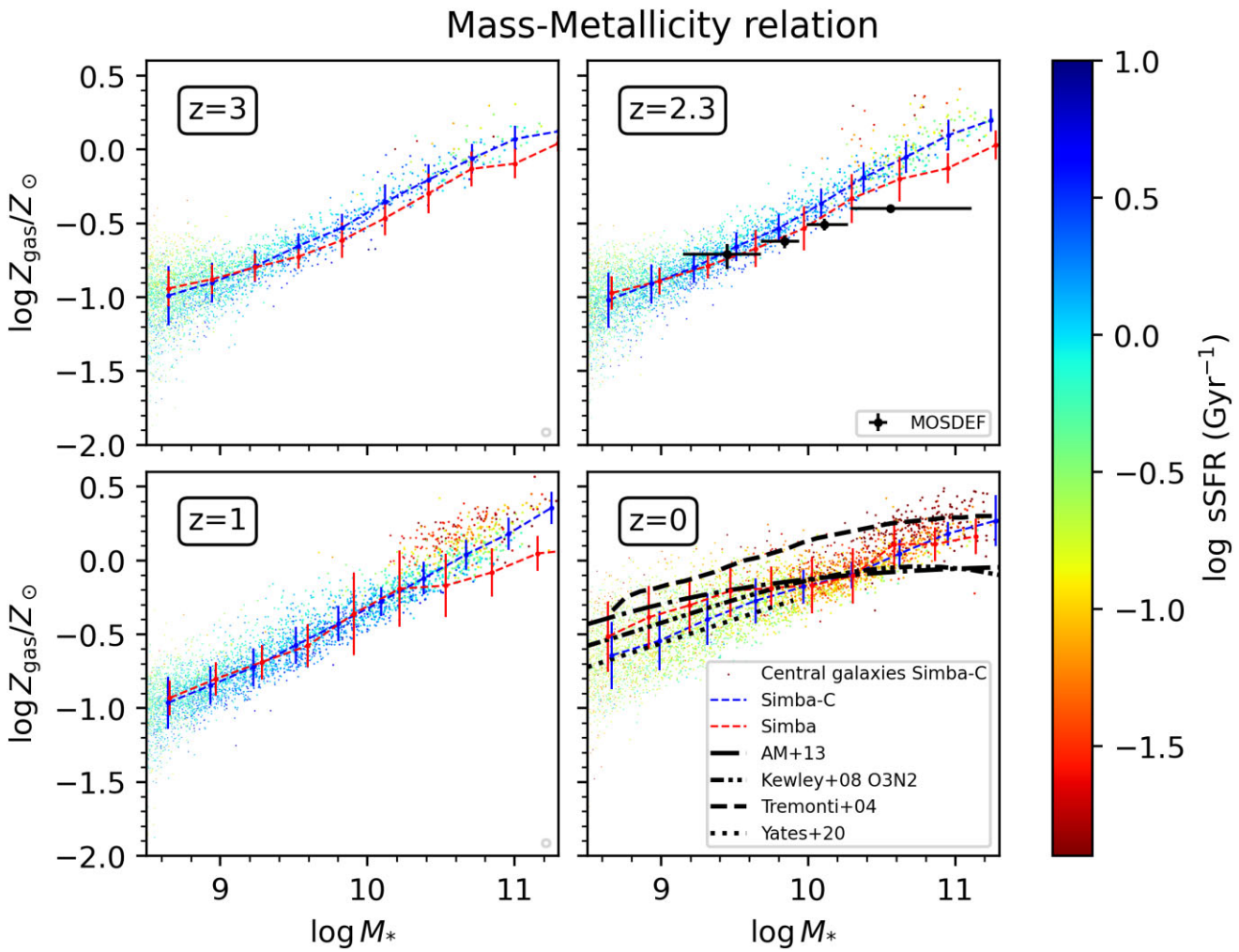

Figure 5. Comparison between the gas-phase mass–metallicity relation (MZR) from $z = 3 \rightarrow 0$ between the median SIMBA-C results shown with the blue line based on its central galaxy values and median SIMBA results shown with the red line. We also compared both simulations with observations from Sanders et al. (2015) (MOSDEF) at $z = 2$ and from Tremonti et al. (2004); Kewley & Ellison (2008); Andrews & Martini (2013); Yates et al. (2020) at $z = 0$. We also include the central galaxy values from the CAESAR galaxy catalogue for the SIMBA-C simulation and scaled their colour to their host galaxy's sSFR. The colour distribution corresponds to blue being star-forming galaxies, while red represents quenched galaxies.

we show the evolution of the MZR from $z = 3$ to $z = 0$. We colour-coded the central galaxies for the SIMBA-C model according to their sSFR and plot the median with a blue line, while showing the median SIMBA result with a red line. We use the observations from Sanders et al. (2015) as part of the Multi-Object Spectrometer for Infra-Red Exploration Deep Evolution Field (MOSDEF) survey at $z = 2.3$. For $z = 0$, we used the results of Tremonti et al. (2004); Kewley & Ellison (2008) and Andrews & Martini (2013), all of whom used the Sloan Digital Sky Survey (SDSS) observations, and Yates et al. (2020) using the Mapping Nearby Galaxies at APO (MaNGA) sample.[9] The total gas-phase metallicity was calculated as an SFR-weighted average of all gas particles in a galaxy, normalized to the solar value of 0.0134 (Asplund et al. 2009). The reason for using an SFR-weighted average is to compare to observations. In observations, (gas) metallicities are measured from nebular emission lines that arise in star-forming regions. Therefore, we only observe the metallicity of the gas that is star-forming. A simple way to account for this is to weigh the metallicity by the SFR of each particle.

Fig. 5 shows that the MZR of the two simulations are very similar between $z = 3$ and $z = 1$, although there are some differences emerging at higher masses between SIMBA and SIMBA-C, albeit not significant. The new model gives a higher total metallicity for the massive galaxies. The most interesting difference between the two simulations is at $z = 0$. The median of the new model is on average lower than that of the SIMBA instantaneous model by $\sim 0.1 - 0.2$ dex. This difference is mostly due to the calibration process explained in Section 2.2. The initial tests showed a very low metallicity count, leading to fewer stars forming. By lowering the strength of the feedback system we were able to produce more stars and higher amounts of metals. However, this came at the cost of the GSMF, which we solved with the wind velocity scaling. Therefore, through trial and error, the best combination between these different components was determined, leading to slightly lower MZR values.

Next, we investigate the stellar mass–metallicity relation, shown in Fig. 6. We plot the relation at $z = 0$ and $z = 2.2$ to directly compare with observations from Gallazzi et al. (2005) who used SDSS-DR2 data, Panter et al. (2008) who analysed the original SDSS data, and

[9]The results from Kewley & Ellison (2008) are the same results as those of Tremonti et al. (2004), but have been refitted using 'strong line metallicities, where we use the calibration of O_3N_2.

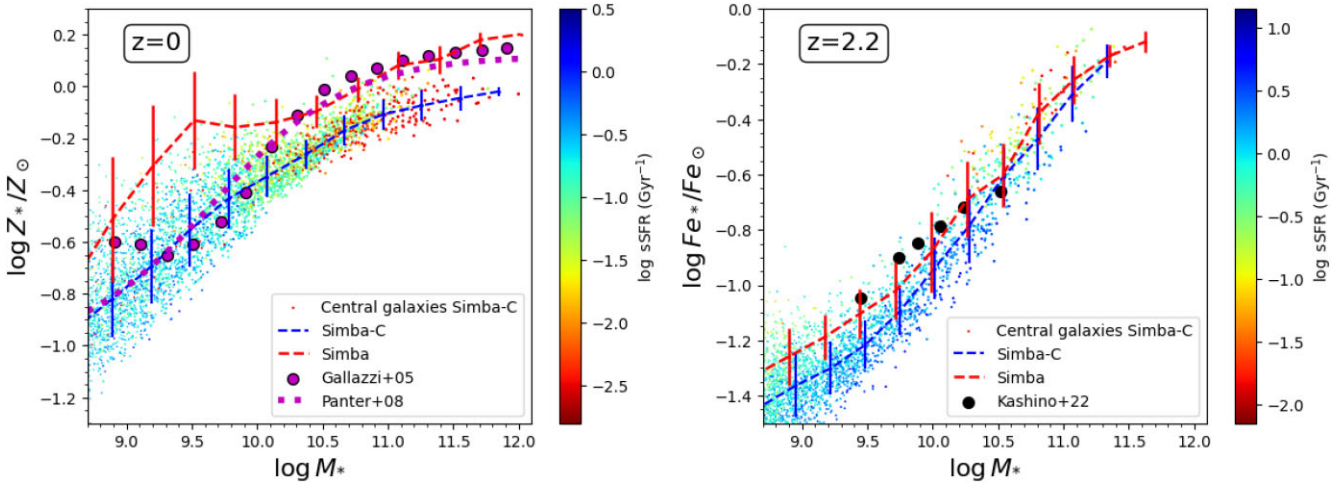

Figure 6. Comparing the stellar mass–metallicity relation at $z = 0$ using the total metallicity abundance (left-hand panel), and at $z = 2.2$ using the iron abundance (right-hand panel) between the median SIMBA-C results shown with the blue line based on its central galaxy values and median SIMBA results shown with the red line. We also compared both simulations with observations from Gallazzi et al. (2005); Panter et al. (2008) at $z \approx 0$ and Kashino et al. (2022) at $z \approx 2.2$. We also include the central galaxy values from the CAESAR galaxy catalogue for the SIMBA-C simulation and scaled their colour to their host galaxy's sSFR. The colour distribution corresponds to blue indicating star-forming galaxies, while red represents quenched galaxies.

Kashino et al. (2022) who used the far-ultraviolet spectra from the high redshift zCOSMOS-deep survey. We again show the comparison plot between the median SIMBA results with a red line, and the median SIMBA-C results shown with a blue line. We also show the sSFR colour-coded distribution of central galaxies, as in Fig. 5. The total and iron stellar metallicity was calculated as an SFR-weighted average of all star particles in a galaxy, normalized to the solar value of 0.0134 (Z) and 1.31×10^{-3} (Fe) (Asplund et al. 2009).

The stellar mass–metallicity results are mostly consistent with the MZR results. The SIMBA-C results are overall $\sim 0.1 - 0.2$ dex lower than the SIMBA results. For $z = 0$ in the lower mass range, the new model matches the observational results, especially Panter et al. (2008), more accurately than SIMBA, while at higher masses SIMBA fares better in this regard. On average, SIMBA-C is more successful in following the general trends of the results of Panter et al. (2008). As for the Gallazzi et al. (2005) results, neither SIMBA or SIMBA-C accurately reproduced the 's'-shaped trend.

On the other hand, at $z = 2.2$, both the SIMBA and SIMBA-C simulation are overall more consistent with the observations than the $z = 0$ result, especially SIMBA. This further confirms that both simulations match the observations, but that the overall trends obtained for both sets of observations are not fully reproduced in the simulations at $z = 0$ and that further investigation of stellar evolution is necessary.

This inconsistency with the trends leads to a discrepancy between the gas-phase MZR and the stellar mass–metallicity, in particular the steepness of the slope at $z = 0$. As mentioned, for the gas-phase mass metallicity (Fig. 5), we obtain a steeper slope for both simulations compared to observations for higher stellar-mass galaxies, while this is not true for the stellar mass metallicity (Fig. 6). Here both simulations obtained a more flat slope compared to the observations, although SIMBA is more comparable to the observations in this mass range. However, this is a discrepancy between the based gas phase (having a steeper slope[10]) and the stellar particles in the simulations (having a more flat slope) might not be related to the same problem.

Possible explanations include: (i) For the gas-phase MZR, the steepness is set by the relationship between a mass loading factor and M_* (see Finlator & Davé 2008; Davé, Finlator & Oppenheimer 2012). Therefore, the assumed mass loading factor scaling with M_* (taken from the FIRE simulation) might be too strong. (ii) also for the gas-phase MZR, at higher masses the slope is sensitive to the type of massive galaxies produced in the simulation. Higher mass star forming galaxies have lower total stellar metallicities than the quenched massive galaxies. Therefore, more massive star-forming galaxies would flatten the slope. This corresponds to our GSFM (Fig. 1) where we did not obtain any star-forming massive galaxies, which resulted in our MZR slope being dominated by the higher total stellar metallicity-valued quenched massive galaxies leading to an increased in the MZR slope. (iii) For stellar mass metallicity, the inaccuracy might be due to using a mass-weighted metallicity for the star particles, whereas in observations it is measured from stellar absorption lines (see Zahid et al. 2013 where they study empirical stellar metallicity models), which can be dominated by AGB stars in quenched galaxies. This might introduce some bias. More research is required to solve this discrepancy.

3.2.2 *Chemical abundances*

In this section, we present the key elemental abundance ratios used to study galactic chemical evolution, to investigate if SIMBA-C is an improvement over SIMBA's previous instantaneous recycling of the metals model assumption.

In Fig. 7, we show the gas-phase oxygen abundance–stellar mass ratio at $z = 0$ (as a proxy for the MZR). We also include the observational results from Tremonti et al. (2004); Kewley & Ellison (2008), who used the SDSS catalogue data release, and the results from Wang & Lilly (2021)'s spectroscopic data from MUSE Atlas of Disks (MAD) and MaNGA.

SIMBA-C produces a lower normalization of the gas-phase oxygen abundance relation than SIMBA. This is similar to the lower MZR for both the gas-phase and the star particles in Figs 5 and

[10]This steeper slope is also seen for the SIMBA-C simulation in Fig. 7.

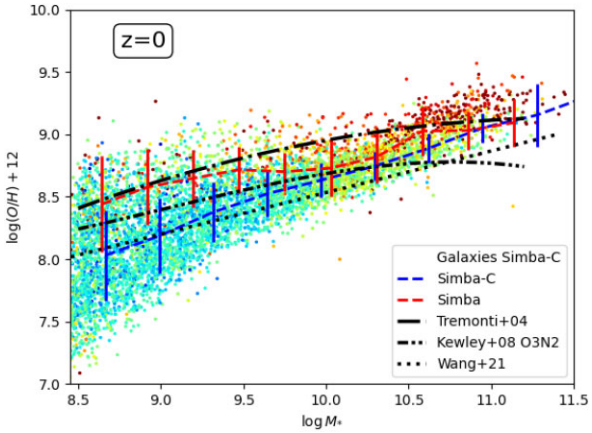

Figure 7. Comparing the gas-phase mass-oxygen abundance relation between the median SIMBA-C results shown with the blue line based on its central galaxy values and median SIMBA results shown with the red line. We also compared both simulations to observations from Tremonti et al. (2004); Kewley & Ellison (2008) using the SDSS catalogue and Wang & Lilly (2021) using the spectroscopic surveys of MAD and MaNGA at $z = 0$. We also include all of the galaxy values from the CAESAR galaxy catalogue for the SIMBA-C simulation and scaled their colour to their host galaxy's sSFR. The colour distribution corresponds to blue indicating star forming galaxies, while red represents quenched galaxies. We use same the solar metallicity normalization of 8.69 for log O/H + 12 used in Tremonti et al. (2004); Asplund et al. (2009); Grevesse et al. (2010).

6. It is interesting to note that at lower galaxy masses, the two simulations follow the two separate observational results. At higher masses, the results converge. In this comparison, the slope of SIMBA is flatter than that of SIMBA-C, unlike in the previous section where both behaved similarly. This can be part of the slope discrepancy discussion in Section 3.2.1, or part of a well-known problem, where the gas-phase mass-oxygen abundance relation MZR is known to differ by as much as ~ 0.7 dex and is not well constrained. A full discussion by Kewley & Ellison (2008), using the fourth release of the SDSS data catalogue, shows that Tremonti et al. (2004) seems to be on the higher end of the mass-oxygen abundance relation. This, together with the fact that Wang & Lilly (2021) uses newer observational results and obtains a lower mass-oxygen abundance relation, indicates a lower value would be more accepted as predicted by SIMBA-C even though it obtained a steeper slope.

In the left-hand panel of Fig. 8, we show the oxygen abundance ratio trend [O/Fe] as a function of metallicity [Fe/H] and, in the right-hand panel, we show the magnesium abundance trend [Mg/Fe].[11] The 2D histograms in the background of both panels show the respective abundance ratios of all the star particles in the SIMBA-C simulation that are in star-forming galaxies of masses $5.0 \times 10^{10}\,\mathrm{M}_\odot < M_* \leq 7.0 \times 10^{10}\,\mathrm{M}_\odot$. Additionally, the long-dashed line shows the median result of SIMBA (with the same selection), while the short-dashed line shows the reproduced results from Kobayashi et al. (2020b). By selecting only these star particles, we try to restrict our results to mimic the results from Kobayashi et al. (2020b), where they use the systematic non-local thermodynamic equilibrium abundances from F and G dwarf stars in the solar neighbourhood (stars within the Milky Way) from observational results of Zhao et al. (2016), to calibrate the original Chem5 model. However, this is not a direct comparison since stars from the solar neighbourhood are not representative of all stars within Milky-Way-like galaxies, but it does give us insight into how each simulation behaves relative to a model calibrated specifically to observations.

The left-hand panel of Fig. 8 shows that the observational data have two segments: (i) a plateau with a slight negative slope at [O/Fe] ~ 0.6 for [Fe/H] $\lesssim -1$, and (ii) a sharp decline from [O/Fe] $\sim$0.6 to [O/Fe] $\sim$0.0 between $-1 \lesssim$ [Fe/H] $\lesssim 0.3$. This well-known pattern (see Wallerstein 1962, for example) can also be seen in the magnesium abundance ratio plot on the right-hand side panel, as predicted by Zhao et al. (2016), who stated that all [α/Fe] ratios will show this pattern. The reason for this pattern is that in the early stages of galaxy formation, only SNe II/HNe contribute, leading to the [O/Fe] plateau across a wide range of [Fe/H] values (Kobayashi et al. 2020b). However, at [Fe/H]~ -1, SNe Ia begins to occur and produces more iron relative to the α elements. The delayed enrichment of SNe Ia then results in the decreasing [α/Fe] ratio. Kobayashi et al. (2020b) incorporated these different interactions, based on the type of SNe, into the Chem5 model to ensure that this characteristic pattern will emerge.

In Fig. 8, we also show the theoretical results of the Chem5 model (blue line) for the abundance of oxygen and magnesium calculated and calibrated in Kobayashi et al. (2020b). By comparing to the theoretical results, we can validate the SIMBA-C model results to the original published Chem5 model that is specifically tested against these abundance ratio trends.

From Fig. 8, we can see that the SIMBA-C simulation (the contour lines) accurately predicts the abundance ratio for both oxygen and magnesium. We have a small negative slope plateau and a clear decrease for both between $-1 <$ [Fe/H] < 0. The decrease seen in the magnesium abundance follows the observations more closely than the oxygen abundance. As for the plateau, both elements have slopes similar to the observations and the theoretical Chem5 model predictions, but unfortunately, the majority of our results do not match the very low [Fe/H] values. However, the plateau still resembles this trend (as expected) but is not part of the majority of the results. This might be due to using all of the stars in Milky-Way-like galaxies and not only solar neighbourhood stars as in the original Chem5 model's calibration.

The SIMBA results are shown in Fig. 8 as a long-dashed line representing the median of the distribution at a given [Fe/H]. It is clear that SIMBA cannot reproduce the trend of the abundance ratio, most likely due to its use of the instantaneous recycling approximation. Therefore, the SIMBA-C simulation is a major improvement over the original SIMBA simulation in that we are now able to accurately predict the abundance ratio trends in Milky-Way-like galaxies.

Finally, in Fig. 9 we show the N/O abundance ratio as a function of the log O/H + 12 metallicity for individual gas particles within star-forming galaxies with stellar masses between[12] $10^9 - 10^{11.5}\,\mathrm{M}_\odot$. We use the three observational data sets presented in Vincenzo & Kobayashi (2018b) as well as their own results (green). These include H II regions in diffused blue dwarf galaxies from Berg et al. (2012); Izotov, Thuan & Guseva (2012); James et al. (2017) (cyan), a higher mass galaxies gas-phase study using the MaNGa spectroscopic survey from Belfiore et al. (2017) (blue) as well as the calculated average from various different stellar and nebulae sources from Izotov & Thuan (1999); Israelian et al. (2004); Spite et al.

[11] We are using the notation [X/Y] to represent the ratio between two elements that have been normalized to solar abundances, namely $\log((X/Y)/(X/Y)_{\mathrm{solar}})$.

[12] We chose this stellar mass range based on the Belfiore et al. (2017) MaNGA observations to allow for direct comparison. It also includes the galaxy stellar mass range used in Vincenzo & Kobayashi (2018b).

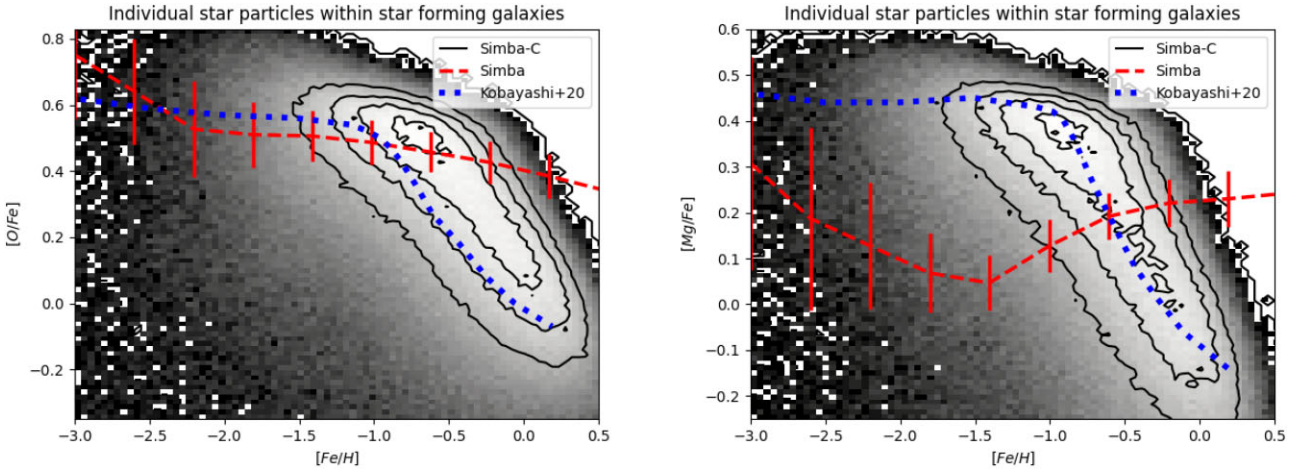

Figure 8. The chemical abundance ratio plots for [O/Fe] versus [Fe/H] (left-hand panel) and [Mg/Fe] versus [Fe/H] (right-hand panel) for stars within Milky-Way-like galaxies. The abundance ratios for the SIMBA-C simulation are shown with contour lines to show the majority of the values. We also included the theoretical model values from Kobayashi et al. (2020b) (blue dotted line), as well as the median SIMBA results (red line).

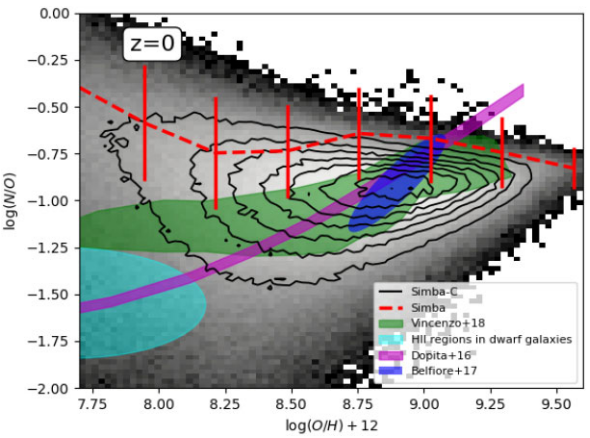

Figure 9. The chemical abundance ratio plot for log N/O versus log O/H + 12 for gas regions within star-forming galaxies with stellar masses between $10^9 - 10^{11.5}\,M_\odot$. The abundance ratios for the SIMBA-C simulation are shown with contour lines, while the median SIMBA values are shown using the red line. For observations, we include the observations presented in Vincenzo & Kobayashi (2018b) (green), from Belfiore et al. (2017) using the MaNGA spectroscopic results (blue), and H II regions in blue diffused dwarf galaxies consisting of various different observations from Berg et al. (2012); Izotov et al. (2012); James et al. (2017) (cyan), and the calculated observational average from Dopita et al. (2016) (magenta). The Dopita et al. (2016) observational average uses observations from both stellar and nebula sources (Izotov & Thuan 1999; Israelian et al. 2004; Spite et al. 2005; Nieva & Przybilla 2012).

(2005); Nieva & Przybilla (2012) as presented in Dopita et al. (2016) (magenta).[13]

Fig. 9 shows a clear difference between SIMBA and the SIMBA-C simulation, with the latter obtaining a lower log N/O value for the region of highest values concentration as a function of log O/H + 12. The SIMBA-C simulation results are in better agreement with observations. With lower values of log N/O, we found that the highest concentration of values within the SIMBA-C coincides with the MaNGA result. This is significant as we limit our results to the stellar mass range of the MaNGA survey. Furthermore, this leads rather elegantly to the fact that the MaNGA survey excludes dwarf galaxy stellar mass ranges (up to a few $10^9\,M_\odot$; Revaz & Jablonka 2018). Since the SIMBA-C result is based on the MaNGA survey's stellar mass range, it is interesting to see that the concentrated levels decrease towards the Dopita et al. (2016) calculated observational average result, but does not quite reach the dwarf galaxy's log N/O versus log O/H + 12 values.[14]

From these comparisons, we can deduce that SIMBA-C shows various improvements over SIMBA, with SIMBA not being able to match either the MaNGA results or the dwarf galaxies. However, neither of the two simulations managed to match the increase in log N/O values as a function of log O/H + 12 (which correlates to the increase in stellar mass), although the SIMBA-C simulation is showing a trend resembling the Dopita et al. (2016) observational average.

We also include the theoretical Chem5 results from the Vincenzo & Kobayashi (2018a) study, which was done on a specific type of galaxy with specifications of $M_* = 3.62 \times 10^{10}\,M_\odot$ for the stellar mass, a gas fraction with respect to the total baryonic mass of $f_{\rm gas} = 0.35$, an average stellar N/O ratio of log N/O $= -0.85$, and lastly that the galaxy is forming stars. Furthermore, the results probe different spatial locations in this galaxy. The results for this galaxy are shown with the green region in Fig. 9. We therefore do not plot the exact same results, but nevertheless, the comparison allows insight into the Chem5 model. Our three highest concentration levels all lie within this region, and our concentrated regions tend in the same direction, albeit with a larger spread. This larger spread in the results is likely due to including a larger stellar mass range.

Vincenzo & Kobayashi (2018b) showed that their results do not match the slope from the observations and postulate that this might

[13]It should be noted that Dopita et al. (2016) also includes individual stellar sources in their average and should therefore be compared with gas-phase metallicity as a function time, unlike integrated stellar abundances of galaxies. Furthermore, they also use the solar normalized value of log O/H + 12 as 9.05, which is different from the solar normalization of 8.69 from Tremonti et al. (2004); Asplund et al. (2009); Grevesse et al. (2010).

[14]We note that when we include dwarf galaxies, our concentration levels did in-fact include the dwarf galaxy region, but shifted our highest concentration of values away from the MaNGA results, while also increasing the spread/uncertainty of our results.

be a consequence of the lack of supersolar metallicity yields from AGB stars not being available;[15] note that supermassive-AGB stars are included in both Chem5 and Vincenzo & Kobayashi (2018a, b). The exact cause needs further investigation.

From the various chemical abundance tests, we can conclude that SIMBA-C shows several improvements over the SIMBA simulation's instantaneous recycling model and that it allows for more accurate chemical enrichment, abundance, and metallicity profile predictions in future work.

4 SUMMARY

In this work we integrated the Chem5 model, developed in Kobayashi et al. (2007), into SIMBA (Davé et al. 2019). The Chem5 model is a set of interpolation tables that determine the mass, energy, and yields from stellar populations based on stellar feedback events, such as stellar winds, AGB winds, SNe Ia, SNe II, and 'failed' SNe. We also introduced the Chabrier IMF into the Chem5 model to match the stellar populations between the Chem5 model and the SIMBA simulation.

We adjusted our modified version of SIMBA, since we were underproducing metals at low redshifts, leading to a low metal cooling efficiency. Due to this, the stellar feedback strength was lowered. This led us to match the global stellar wind feedback velocity normalization of Muratov et al. (2015). We also improved the GSMF compared to the SIMBA simulation, especially at $z = 0$. No direct tuning of the metallicities was performed. We only used its results to calibrate the simulation's SFR to the new model.

Other notable results include an improved sSFR–stellar mass relation for the low-and high-mass ranges while producing fewer galaxies in the green valley at intermediate masses, in better accordance with observational data. Furthermore, SIMBA-C shows improvements across all galaxy mass ranges in terms of the black hole–stellar mass relation relative to SIMBA in evolving black holes within low-mass galaxies, although this contributed to the new black hole seeding and growth implementation rather than the Chem5 model.

In terms of the metal content predicted by the new Chem5 model, SIMBA-C was able to reproduce the observational data on almost all levels except for the stellar mass–metallicity relation at the highest galaxy masses. The new model will enable us to study individual chemical abundance more robustly. These include an improved agreement in the [O/Fe] and [Mg/Fe] versus [Fe/H] for stars within Milky-Way-like galaxies and a better match to observations of log N/O versus log O/H + 12.

Future work will investigate how to extend the α-abundance ratios to have a more distinct plateau for [Fe/H]<-1.0, as well as trying to constrain the large spread in the values of log N/O that occurs at low log O/H + 12. Finally, we will continue to make improvements to the SIMBA-C model such as including SIMBA's dust model and explore how to alleviate SIMBA-C's discrepancies with the gas-phase metal content of the high-mass galaxies.

We conclude that the integration of the new chemical enrichment model and other changes of the SIMBA-C model yields significant improvements over SIMBA. Moreover, the new model includes all elements from H $\rightarrow$ Ge, rather than just the standard 11 elements of stellar evolution. Chem5 accounts for state-of-the-art enrichment processes such as 'failed' SNe, super AGB, and HNe to generate these additional elements. These advances open up new avenues for constraining chemical evolution processes within galaxies and circumgalactic and intergalactic gas, which we will explore in future work.

[15]Nitrogen is mostly synthesized by intermediate-mass stars by hot bottom burning during the AGB phase, while oxygen is mostly produced by core-collapse SNe with short lifetimes ($\sim 10^6$ yr) (Vincenzo & Kobayashi 2018b).

ACKNOWLEDGEMENTS

This work is based on research supported in part by the National Research Foundation of South Africa (NRF Grant Number: 146053). The analysis reported in this article was enabled by HPC resources provided by WestGrid and Digital Research Alliance of Canada (alliancecan.ca) award to AB. RH also acknowledges the SIMBA collaboration for the use of the simulation. RH also acknowledges the Royal Society of Science travel grant that allowed for in-person collaboration at the University of Edinburgh, Scotland, to further this study. AB and DR acknowledge support from the Natural Sciences and Engineering Research Council of Canada (NSERC) through its Discovery Grant program. Also, AB acknowledges support from the Infosys Foundation via an endowed Infosys Visiting Chair Professorship at the Indian Institute of Science. Additionally, AB acknowledges the lək$^{\text{w}}$əŋən peoples on whose traditional territory the University of Victoria stands, and the Songhees, Equimalt, and WSÁNEĆ peoples whose historical relationships with the land continue to this day. Any opinion, finding, and conclusion or recommendation expressed in this material is that of the author(s), and the NRF does not accept any liability in this regard. WC is supported by the STFC AGP Grant ST/V000594/1, the Atracción de Talento Contract no. 2020-T1/TIC-19882 granted by the Comunidad de Madrid in Spain and the Project grant PID2021-122603NB-C21 from the Ministerio de Ciencia e Innovación, Spain. CK acknowledges funding from the UK Science and Technology Facility Council (STFC) through grant ST/R000905/1 and ST/V000632/1. The authors thank the anonymous reviewer for constructive comments that led to the improvement of the article.

DATA AVAILABILITY

The published SIMBA simulation (Davé et al. 2019) is available on the SIMBA university repository at http://simba.roe.ac.uk/. The SIMBA-C simulation data underlying this article will be shared on reasonable request to the corresponding author.

REFERENCES

Abel T., Bryan G. L., Norman M. L., 2002, Science, 295, 93
Alonso Asensio I., Dalla Vecchia C., Potter D., Stadel J., 2023, MNRAS, 519, 300
Andrews B. H., Martini P., 2013, ApJ, 765, 140
Anglés-Alcázar D., Davé R., Faucher-Giguère C.-A., Özel F., Hopkins P. F., 2017a, MNRAS, 464, 2840
Anglés-Alcázar D., Faucher-Giguère C.-A., Kereš D., Hopkins P. F., Quataert E., Murray N., 2017b, MNRAS, 470, 4698
Asplund M., Grevesse N., Sauval A. J., Scott P., 2009, ARA&A, 47, 481
Baldry I. K. et al., 2012, MNRAS, 421, 621
Belfiore F. et al., 2017, MNRAS, 469, 151
Benson A. J., Babul A., 2009, MNRAS, 397, 1302
Bentz M. C., Manne-Nicholas E., 2018, ApJ, 864, 146
Berg D. A. et al., 2012, ApJ, 754, 98
Bernardi M., Meert A., Sheth R. K., Fischer J. L., Huertas-Company M., Maraston C., Shankar F., Vikram V., 2017, MNRAS, 467, 2217
Bertschinger E., 1998, ARA&A, 36, 599
Best P. N., Heckman T. M., 2012, MNRAS, 421, 1569

Beverage A. G., Kriek M., Conroy C., Sandford N. R., Bezanson R., Franx M., van der Wel A., Weisz D. R., 2023,ApJ, 948, 140
Bondi H., 1952, MNRAS, 112, 195
Bromm V., Coppi P. S., Larson R. B., 2002, ApJ, 564, 23
Cameron A. G. W., Truran J. W., 1971, J. R. Astron. Soc. Can., 65, 1
Ceverino D., Klypin A., 2009, ApJ, 695, 292
Chabrier G., 2003, PASP, 115, 763
Choi E., Ostriker J. P., Naab T., Johansson P. H., 2012, ApJ, 754, 125
Conroy C., Graves G. J., van Dokkum P. G., 2014, ApJ, 780, 33
Conroy C., van Dokkum P. G., Kravtsov A., 2015, ApJ, 803, 77
Cui W. et al., , 2022, MNRAS, 514, 977
Davé R., Anglés-Alcázar D., Narayanan D., Li Q., Rafieferantsoa M. H., Appleby S., 2019, MNRAS, 486, 2827
Davé R., Finlator K., Oppenheimer B. D., 2012, MNRAS, 421, 98
Davé R., Oppenheimer B. D., Finlator K., 2011, MNRAS, 415, 11
Davé R., Thompson R., Hopkins P. F., 2016, MNRAS, 462, 3265
Doherty C. L., Gil-Pons P., Lau H. H. B., Lattanzio J. C., Siess L., 2014a, MNRAS, 437, 195
Doherty C. L., Gil-Pons P., Lau H. H. B., Lattanzio J. C., Siess L., Campbell S. W., 2014b, MNRAS, 441, 582
Doherty C. L., Gil-Pons P., Siess L., Lattanzio J. C., 2017, Publ. Astron. Soc. Austr., 34, e056
Dolag K., Borgani S., Schindler S., Diaferio A., Bykov A. M., 2008, Space Sci. Rev., 134, 229
Dopita M. A., Kewley L. J., Sutherland R. S., Nicholls D. C., 2016, Ap&SS, 361, 61
Faber S. M. et al., 2007, ApJ, 665, 265
Fabian A. C., 2012, ARA&A, 50, 455
Finlator K., Davé R., 2008, MNRAS, 385, 2181
Frischknecht U. et al., 2016, MNRAS, 456, 1803
Gallazzi A., Charlot S., Brinchmann J., White S. D. M., Tremonti C. A., 2005, MNRAS, 362, 41
Grevesse N., Asplund M., Sauval A. J., Scott P., 2010, Ap&SS, 328, 179
Grevesse N., Noels A., Sauval A. J., 1996, in Holt S. S., Sonneborn G.eds, ASP Conf. Ser. Vol. 99, Cosmic Abundances. Astron. Soc. Pac., San Francisco, p. 117
Haardt F., Madau P., 2012, ApJ, 746, 125
Hahn O., Abel T., 2011, MNRAS, 415, 2101
Heckman T. M., Best P. N., 2014, ARA&A, 52, 589
Hirschmann M., De Lucia G., Fontanot F., 2016, MNRAS, 461, 1760
Hopkins P. F., 2015, MNRAS, 450, 53
Hopkins P. F., 2017, preprint (arXiv:1712.01294)
Hopkins P. F., Quataert E., 2011, MNRAS, 415, 1027
Hopkins P. F., Quataert E., Murray N., 2012, MNRAS, 421, 3522
Hopkins P. F., Wellons S., Anglés-Alcázar D., Faucher-Giguère C.-A., Grudić M. Y., 2022, MNRAS, 510, 630
Hough R., Rennehan D., Loubser S. I., Babul A., Davé R., 2021, in The Proceedings of SAIP2021, The 65th Annual Conference of the South African Institute of Physics. South African Institute of Physics, Johannesburg, p. 328
Ibrahim D., Kobayashi C., 2023, preprint (arXiv:2307.11595)
Israelian G., Ecuvillon A., Rebolo R., García-López R., Bonifacio P., Molaro P., 2004, A&A, 421, 649
Iwamoto K., Brachwitz F., Nomoto K., Kishimoto N., Umeda H., Hix W. R., Thielemann F.-K., 1999, ApJS, 125, 439
Izotov Y. I., Thuan T. X., 1999, ApJ, 511, 639
Izotov Y. I., Thuan T. X., Guseva N. G., 2012, A&A, 546, A122
James B. L., Koposov S. E., Stark D. P., Belokurov V., Pettini M., Olszewski E. W., McQuinn K. B. W., 2017, MNRAS, 465, 3977
Janka H.-T., 2012, Annu. Rev. Nucl. Part. Sci., 62, 407
Jetha N. N., Hardcastle M. J., Babul A., O'Sullivan E., Ponman T. J., Raychaudhury S., Vrtilek J., 2008, MNRAS, 384, 1344
Jung S. L. et al., 2022, MNRAS, 515, 22
Kashino D. et al., 2022, ApJ, 925, 82
Kennicutt Robert C.J. et al., 2007, ApJ, 671, 333
Kennicutt Robert C.J., 1998, ApJ, 498, 541
Kewley L. J., Ellison S. L., 2008, ApJ, 681, 1183
Kobayashi C. et al., 2023, ApJ, 943, L12
Kobayashi C., 2004, MNRAS, 347, 740
Kobayashi C., Arimoto N., 1999, ApJ, 527, 573
Kobayashi C., Karakas A. I., Lugaro M., 2020b, ApJ, 900, 179
Kobayashi C., Karakas A. I., Umeda H., 2011, MNRAS, 414, 3231
Kobayashi C., Leung S.-C., Nomoto K., 2020a, ApJ, 895, 138
Kobayashi C., Nakasato N., 2011, ApJ, 729, 16
Kobayashi C., Nomoto K., 2009, ApJ, 707, 1466
Kobayashi C., Springel V., White S. D. M., 2007, MNRAS, 376, 1465
Kobayashi C., Taylor P., 2023, preprint (arXiv:2302.07255)
Kobayashi C., Tsujimoto T., Nomoto K., 2000, ApJ, 539, 26
Kobayashi C., Tsujimoto T., Nomoto K., Hachisu I., Kato M., 1998, ApJ, 503, L155
Kobayashi C., Umeda H., Nomoto K., Tominaga N., Ohkubo T., 2006, ApJ, 653, 1145
Kormendy J., Ho L. C., 2013, ARA&A, 51, 511
Krumholz M. R., Gnedin N. Y., 2011, ApJ, 729, 36
Lagos P. et al., 2022, MNRAS, 516, 5487
Larson R. B., 1974, MNRAS, 169, 229
Leroy A. K., Walter F., Brinks E., Bigiel F., de Blok W. J. G., Madore B., Thornley M. D., 2008, AJ, 136, 2782
Liang L., Durier F., Babul A., Davé R., Oppenheimer B. D., Katz N., Fardal M., Quinn T., 2016, MNRAS, 456, 4266
Limongi M., Chieffi A., 2018, ApJS, 237, 13
Limongi M., Chieffi A., Bonifacio P., 2003, ApJ, 594, L123
Madau P., Dickinson M., 2014, ARA&A, 52, 415
Maiolino R., Mannucci F., 2019, A&AR, 27, 3
Maoz D., Graur O., 2017, ApJ, 848, 25
Marek A., Janka H. T., 2009, ApJ, 694, 664
Matteucci F., 1994, A&A, 288, 57
Matteucci F., 2016, J. Phys. Conf. Ser., 703, 012004
McDermid R. M. et al., 2015, MNRAS, 448, 3484
McNamara B. R., Nulsen P. E. J., 2007, ARA&A, 45, 117
Mehta V. et al., 2017, ApJ, 838, 29
Muratov A. L., Kereš D., Faucher-Giguère C.-A., Hopkins P. F., Quataert E., Murray N., 2015, MNRAS, 454, 2691
Muzzin A. et al., 2013, ApJ, 777, 18
Naab T., Ostriker J. P., 2017, ARA&A, 55, 59
Nieva M. F., Przybilla N., 2012, A&A, 539, A143
Nomoto K., Hashimoto M., Tsujimoto T., Thielemann F. K., Kishimoto N., Kubo Y., Nakasato N., 1997, Nucl. Phys. A., 616, 79
Nomoto K., Kobayashi C., Tominaga N., 2013, ARA&A, 51, 457
Nomoto K., Tominaga N., Umeda H., Kobayashi C., Maeda K., 2006, Nucl. Phys. A., 777, 424
Oppenheimer B. D., Babul A., Bahé Y., Butsky I. S., McCarthy I. G., 2021, Universe, 7, 209
Oppenheimer B. D., Davé R., 2006, MNRAS, 373, 1265
Panter B., Jimenez R., Heavens A. F., Charlot S., 2008, MNRAS, 391, 1117
Perna M., Lanzuisi G., Brusa M., Mignoli M., Cresci G., 2017, A&A, 603, A99
Piontek F., Steinmetz M., 2011, MNRAS, 410, 2625
Planck Collaboration VI 2018, A&A, 641, A6
Pokhrel R. et al., 2021, ApJ, 912, L19
Rahmati A., Pawlik A. H., Raičević M., Schaye J., 2013, MNRAS, 430, 2427
Rasia E. et al., 2015, ApJ, 813, L17
Rennehan D., Babul A., Hayward C. C., Bottrell C., Hani M. H., Chapman S. C., 2020, MNRAS, 493, 4607
Revaz Y., Jablonka P., 2018, A&A, 616, A96
Romano D., Calura F., D'Ercole A., Few C. G., 2019, A&A, 630, A140
Romano D., Chiappini C., Matteucci F., Tosi M., 2005, A&A, 430, 491
Salim S., Boquien M., Lee J. C., 2018, ApJ, 859, 11
Sanders R. L. et al., 2015, ApJ, 799, 138
Scannapieco E., Bildsten L., 2005, ApJ, 629, L85
Sherman S. et al., 2020, MNRAS, 499, 4239
Smith B. D. et al., 2017, MNRAS, 466, 2217
Smith B. D., Turk M. J., Sigurdsson S., O'Shea B. W., Norman M. L., 2009, ApJ, 691, 441
Smith B., Sigurdsson S., Abel T., 2008, MNRAS, 385, 1443
Somerville R. S., Davé R., 2015, ARA&A, 53, 51

Song M. et al., 2016, ApJ, 825, 5
Spite M. et al., 2005, A&A, 430, 655
Spolaor M., Kobayashi C., Forbes D. A., Couch W. J., Hau G. K. T., 2010, MNRAS, 408, 272
Springel V., 2005, MNRAS, 364, 1105
Springel V., Frenk C. S., White S. D. M., 2006, Nature, 440, 1137
Stinson G. S., Brook C., Macciò A. V., Wadsley J., Quinn T. R., Couchman H. M. P., 2013, MNRAS, 428, 129
Sturm E. et al., 2011, ApJ, 733, L16
Taylor P., Kobayashi C., 2014, MNRAS, 442, 2751
Thomas D., Maraston C., Bender R., Mendes de Oliveira C., 2005, ApJ, 621, 673
Thomas N., Davé R., Jarvis M. J., Anglés-Alcázar D., 2021, MNRAS, 503, 3492
Tomczak A. R. et al., 2014, ApJ, 783, 85
Tremonti C. A. et al., 2004, ApJ, 613, 898
Umeda H., Nomoto K., 2002, ApJ, 565, 385
Vincenzo F., Kobayashi C., 2018a, MNRAS, 478, 155
Vincenzo F., Kobayashi C., 2018b, A&A, 610, L16
Vogelsberger M., Marinacci F., Torrey P., Puchwein E., 2020, Nat. Rev. Phys., 2, 42
Wallerstein G., 1962, ApJS, 6, 407
Wang E., Lilly S. J., 2021, ApJ, 910, 137
White S. D. M., Frenk C. S., 1991, ApJ, 379, 52
Woosley S. E., Weaver T. A., 1995, ApJS, 101, 181
Yates R. M., Henriques B. M. B., Fu J., Kauffmann G., Thomas P. A., Guo Q., White S. D. M., Schady P., 2021, MNRAS, 503, 4474
Yates R. M., Schady P., Chen T. W., Schweyer T., Wiseman P., 2020, A&A, 634, A107
Yu Q., Tremaine S., 2002, MNRAS, 335, 965
Zahid H. J., Geller M. J., Kewley L. J., Hwang H. S., Fabricant D. G., Kurtz M. J., 2013, ApJ, 771, L19
Zhao G. et al., 2016, ApJ, 833, 225

This paper has been typeset from a TEX/LATEX file prepared by the author.